RHOA[L57V] drives the development of diffuse gastric cancer through IGF1R-PAK1-YAP1 signaling

Antje Schaefer[1,2,*], Richard G. Hodge[1], Haisheng Zhang[3,‡], G. Aaron Hobbs[1,2,†], Julien Dilly[4], Minh Huynh[5], Craig M. Goodwin[1], Feifei Zhang[3], J. Nathaniel Diehl[6], Mariaelena Pierobon[7], Elisa Baldelli[7], Sehrish Javaid[8], Karson Guthrie[1], Naim U. Rashid[1,9], Emanuel F. Petricoin[7], Adrienne D. Cox[1,2,8,10], William C. Hahn[4,11,12,13], Andrew J. Aguirre[4,11,12,13], Adam J. Bass[3,13,14,*], Channing J. Der[1,2,6,8,*]

[1]Lineberger Comprehensive Cancer Center, University of North Carolina at Chapel Hill, Chapel Hill, NC 27599, USA.

[2]Department of Pharmacology, University of North Carolina at Chapel Hill, Chapel Hill, NC 27599, USA.

[3]Division of Molecular and Cellular Oncology, Dana-Farber Cancer Institute, Boston, MA 02215, USA.

[4]Department of Medical Oncology, Dana-Farber Cancer Institute, Boston, MA 02215, USA.

[5]Department of Biochemistry and Biophysics, University of North Carolina at Chapel Hill, Chapel Hill, NC 27599, USA.

[6]Curriculum in Genetics and Molecular Biology, University of North Carolina at Chapel Hill, Chapel Hill, NC 27599, USA.

[7]Center for Applied Proteomics and Molecular Medicine, School of Systems Biology, George Mason University, Manassas, VA 20110, USA.

[8]Program in Oral and Craniofacial Biomedicine, University of North Carolina at Chapel Hill, Chapel Hill, NC 27599, USA.

[9]Department of Biostatistics, Gillings School of Global Public Health, University of North Carolina at Chapel Hill, Chapel Hill, NC 27599, USA.

[10]Department of Radiation Oncology, University of North Carolina at Chapel Hill, Chapel Hill, NC 27599, USA.

[11]Department of Medicine, Brigham and Women's Hospital and Harvard Medical School, Boston, MA 02115, USA.

[12]Harvard Medical School, Boston, MA 02115, USA.

[13]Cancer Program, Broad Institute of MIT and Harvard, Cambridge, MA 02142, USA.

[14]Herbert Irving Comprehensive Cancer Center at Columbia University, New York, NY 10032, USA.

Abstract

Cancer-associated mutations in the guanosine triphosphatase (GTPase) RHOA are found at different locations from the mutational hotspots in the structurally and biochemically related RAS. Tyr^{42}-to-Cys (Y42C) and Leu^{57}-to-Val (L57V) substitutions are the two most prevalent RHOA mutations in diffuse gastric cancer (DGC). $RHOA^{Y42C}$ exhibits a gain-of-function phenotype and is an oncogenic driver in DGC. Here, we determined how $RHOA^{L57V}$ promotes DGC growth. In mouse gastric organoids with deletion of *Cdh1*, which encodes the cell adhesion protein E-cadherin, the expression of $RHOA^{L57V}$, but not of wild-type RHOA, induced an abnormal morphology similar to that of patient-derived DGC organoids. $RHOA^{L57V}$ also exhibited a gain-of-function phenotype and promoted F-actin stress fiber formation and cell migration. $RHOA^{L57V}$ retained interaction with effectors but exhibited impaired RHOA intrinsic and GAP-catalyzed GTP hydrolysis, which favored formation of the active GTP-bound state. Introduction of missense mutations at KRAS residues analogous to Tyr^{42} and Leu^{57} in RHOA did not activate KRAS oncogenic potential, indicating distinct functional effects in otherwise highly related GTPases. Both RHOA mutants stimulated the transcriptional co-activator YAP1 through actin dynamics to promote DGC progression; however, $RHOA^{L57V}$ additionally did so by activating the kinases IGF1R and PAK1, distinct from the FAK-mediated mechanism induced by $RHOA^{Y42C}$. Thus, $RHOA^{L57V}$ and $RHOA^{Y42C}$ drive the development of DGC through distinct signaling mechanisms.

INTRODUCTION

The RAS homologous (RHO) small guanosine triphosphatases (GTPases; such as RHOA and RAC1) function as signaling nodes that relay extracellular signals to cytoplasmic signaling networks that control diverse cellular processes (1–4). RHOA acts as a molecular on-off binary switch that cycles between active guanosine triphosphate (GTP)-bound and inactivate guanosine diphosphate (GDP)-bound states. Whereas RHOA-selective guanine nucleotide exchange factors (GEFs) stimulate intrinsic GDP-GTP nucleotide exchange to promote RHOA-GTP formation, RHOA-selective GTPase-activating proteins (GAPs) accelerate intrinsic GTP hydrolysis activity and formation of inactive RHOA-GDP. Guanine nucleotide dissociation inhibitors (GDIs) interact with geranylgeranyl lipid-modified and membrane-associated RHOA and sequester the GTPase in the cytosol, preventing RHOA activation and promoting degradation. Active GTP-bound RHOA binds to a functionally diverse spectrum of effectors to regulate signaling networks that control actin-mediated processes that include cell motility, cell adhesion, and cell cycle progression (5, 6).

Mutationally activated *RAS* genes (*H/K/NRAS*) were identified in cancer four decades ago and comprise the most frequently mutated oncogene family in a diverse spectrum of cancer types (7–9). Missense mutations in RAS occur predominantly at codons encoding Gly[12], Gly[13], and Gln[61] (commonly known and referred to hereafter as G12, G13, and Q61, respectively) with mutation- and tissue-specific differences in their frequencies and biological functions (10–12). In contrast, cancer-associated missense mutations in RHOA and RAC1 were identified only recently and are found in a very restricted set of cancer types (13–16). Additionally, despite the conservation of amino acid residues corresponding to RAS mutational hotspots, surprisingly, cancer-associated *RHOA* and *RAC1* mutations are found at strikingly different residues (16).

Gastric cancer is the fifth most common malignancy and the third leading cause of cancer death worldwide (17). Diffuse gastric cancer (DGC) is the most aggressive, lethal variant of gastric cancer (18, 19). DGC lacks clinically effective therapies in part because the molecular mechanisms driving DGC tumorigenesis are not well characterized. One of the most frequent genetic events in DGC is the somatic inactivation of the canonical tumor suppressor *CDH1* (18–20), encoding the cell adhesion protein E-cadherin that regulates the cell-cell adhesion, mobility, and proliferation of epithelial cells (21). Full exome sequencing studies identified *RHOA* mutations in 15–26% of DGC that often co-occur with *CDH1* loss (18–20, 22). The most prevalent *RHOA* mutations in DGC encode Y42C and L57V amino acid substitutions, and both are found at locations distinct from cancer-associated *RAS* and *RAC1* alterations (16). We previously determined that RHOA[Y42C] acts as an oncogenic, gain-of-function mutant in DGC (23). Expression of RHOA[Y42C], together with *CDH1* loss, induced DGC growth through focal adhesion kinase (FAK)-mediated activation of PI3K-AKT-β-catenin and YAP1 signaling. RHOA[Y42C] promoted metastasis, cell proliferation, and an immunosuppressive tumor microenvironment (23, 24). Mechanistically, RHOA[Y42C] exhibited impaired GTP hydrolysis activities, favoring the formation of the active GTP-bound state, and additionally showed impaired effector binding (23).

The L57V substitution occurs in a different region in RHOA than Y42C, suggesting that these mutations induce distinct consequences for RHOA function. The Leu[57] residue is located adjacent to the flexible switch II region which is involved in binding of regulatory proteins and effectors (2). However, the role of Leu[57] in RHOA wild-type (RHOA[WT]) binding to GDP/GTP, regulatory proteins or effectors is unknown. Leu[57] is conserved among RHOA, RAC1 and RAS (fig. S1A), yet Leu[57] alterations in cancer have been described only for RHOA. Mutations at analogous residues in RAS or other RHO family proteins, which would enable extrapolation of the consequences of a mutated Leu[57] residue, have not been described. In contrast to the *RAS* oncogenes and even to other cancer-associated *RHOA* mutations, only one Leu[57] substitution (L57V) has been found in cancer, although five different single-base substitutions are hypothetically possible (fig. S1B), emphasizing the potentially unique function of RHOA[L57V]. Our understanding of RHOA[L57V] as a driver of DGC is limited. RHOA[L57V] has been shown to cause a loss-of-function phenotype because of impaired binding to the effector Rhotekin in pulldown studies (20), a standard approach to measure RHOA-GTP levels in cells. However, the same study also found that RHOA[L57V] stimulated organoid growth, suggesting a gain-of-function phenotype. One possible explanation for these conflicting results is that the L57V mutation may impair

binding to Rhotekin but not to other effectors, similar to what we found for RHOA^{Y42C} (23). If so, the Rhotekin pulldown approach would not correctly reflect the active GTP levels of RHOA^{L57V}. It remains to be identified which biochemical and signaling consequences RHOA^{L57V} induces for RHOA function and whether RHOA^{L57V} acts as gain- or loss-of-function mutation in driving DGC tumorigenesis.

In this study, we characterized the consequences of the L57V substitution on RHOA function. We determined that, like Y42C, L57V also caused a gain-of-function phenotype and promoted DGC development. However, each mutant exhibited distinct biochemical alterations and stimulated distinct signaling activities, but both converged on YAP1 activation. Finally, saturation mutagenesis of KRAS at residues analogous to RHOA Tyr^{42} and Leu^{57} did not lead to oncogenic activation, providing a basis for the distinct mutational paths that RHOA and RAS take in human carcinogenesis.

RESULTS

RHOA^{L57V} disrupts the morphology of gastric organoids and induces a DGC-like phenotype

Y42C and L57V comprise the two most prevalent (each at 21%) *RHOA* mutations in DGC (16). However, they are found in divergent structural regions of RHOA, suggesting that they cause distinct consequences for RHOA function (Fig. 1A and fig. S1A). To study the role of RHOA^{L57V} in DGC development, we applied an experimental approach that we described previously to evaluate the activity of the DGC-associated RHOA^{Y42C} mutant (23).

We generated a mouse-derived gastric organoid model in which we induced lentiviral mediated exogenous expression of RHOA^{L57V} together with tamoxifen-mediated loss of the endogenous canonical tumor suppressor *Cdh1*, the most common genetic event in DGC (18–20). In mice, we introduced the *Mist1*CreERT2 allele encoding tamoxifen-induced Cre recombinase in the *Mist1* locus (Fig. 1B), which is a marker of gastric chief cells expressed in isthmus stem cells (25–27). In addition, we added the conditional *Cdh1* allele (*Cdh1$^{Flox/Flox}$*) and the R26mTmG 'Tomato-GFP' allele which allowed identification of Cre-recombined cells by their change from red (tomato) to green (GFP) fluorescence. We isolated gastric organoids and induced *Cdh1* loss in vitro by the addition of tamoxifen. *Cdh1* deletion was directly verified by loss of E-cadherin protein expression (Fig. 1C). Next, we stably expressed HA-epitope-tagged RHOA^{WT} or RHOA^{L57V} in *Cdh1$^{-/-}$* organoids using lentiviral expression vectors (Fig. 1B). After selecting for mass populations of puromycin-resistant cells, the expression of each RHOA variant was confirmed by immunoblot analyses. The HA-tagged RHOA WT and L57V proteins were expressed at comparable levels (Fig. 1D) and comparable to endogenous RHOA expression (fig. S1, C and D).

When we ectopically expressed RHOA^{WT} or control empty vector (EV) in *Cdh1$^{-/-}$* organoids, the organoids retained their spherical forms with hollow interiors (Fig. 1, E to G). In contrast, expression of RHOA^{L57V} disrupted the symmetric organoid morphology and induced central filling. This phenotype is associated with cellular transformation and similar to that observed in DGC patient-derived organoids (23, 28, 29). Histologic analyses by hematoxylin and eosin (H&E) staining to visualize nuclei and cytoplasm/extracellular

matrix, respectively, confirmed that $Cdh1^{-/-}$ organoids expressing RHOA^{L57V}, but not RHOA^{WT} or empty vector, exhibited signet-ring cells (Fig. 1F), a characteristic histologic feature of DGC. The presence of signet-ring cells was further verified and quantitated by positive alcian blue staining for mucin expression (Fig. 1G, fig. S1E) (23, 30). In summary, RHOA^{L57V} together with $Cdh1$ loss caused an abnormal morphology of gastric organoids, comparable to the phenotype we observed with RHOA^{Y42C} in $Cdh1$-null gastric organoids (23), and induced a similar phenotype as observed in DGC patients.

RHOA^{L57V} is a gain-of-function mutant that promotes F-actin stress fiber formation and cell migration

We next assessed whether the L57V mutation caused a gain-of-function RHOA phenotype. The best characterized cellular function associated with RHOA activation is the stimulation of actin stress fibers (1–4). Previous studies showed that lab-generated constitutively activated RHOA with mutations (G14V and Q63L) at residues analogous to cancer-associated RAS alterations (fig. S1A) showed gain-of-function cellular phenotypes when ectopically expressed in NIH/3T3 and Swiss 3T3 mouse fibroblast cell lines (31–33). To determine if the L57V substitution causes a comparable gain-of-function, we stably expressed RHOA^{L57V} in NIH/3T3 cells (Fig. 2, A and B). We first evaluated the ability of RHOA^{L57V} to stimulate F-actin stress fiber formation. Consistent with previous findings (34), RHOA^{Q63L} but not WT expressing NIH/3T3 cells showed increased formation of F-actin stress fibers (Fig. 2, C and D, fig. S1F). Similar to what we observed with RHOA^{Y42C} (23), RHOA^{L57V} also stimulated comparable development of F-actin stress fibers to levels intermediate between that seen with RHOA^{Q63L} and RHOA^{WT}.

Next, we analyzed the effects of RHOA^{L57V} on cell adhesion to the extracellular matrix, a RHOA-dependent activity promoted by stress fiber formation (6, 35). As we described previously (23), expression of RHOA^{WT} and RHOA^{Q63L} reduced NIH/3T3 cell adhesion to fibronectin (Fig. 2E). In contrast, RHOA^{L57V}, as we observed with RHOA^{Y42C} (23), also did not alter cell-matrix adhesion.

Finally, we evaluated the consequences of RHOA^{L57V} on random cell migration, a process also linked to RHOA-mediated induction of stress fiber formation (6, 35). As we and others described previously (23, 36, 37), RHOA^{Q63L} but not RHOA^{WT} decreased the migration velocity of NIH/3T3 cells (Fig. 2F), whereas like RHOA^{Y42C}, RHOA^{L57V} expressing fibroblasts showed increased velocity. In summary, RHOA^{L57V} induces a gain-of-function phenotype that is distinct from the lab-generated constitutively activated RHOA^{Q63L} mutant and, instead, is comparable to the cellular activities seen with the DGC-associated RHOA^{Y42C} mutant (23).

RHOA^{L57V} exhibits impaired GTP hydrolysis activities

We next sought to identify the molecular basis for our observed cellular phenotypes of the gain-of-function RHOA^{L57V} mutant. The Leu^{57} residue is localized adjacent to the switch II region and is highly conserved among the RHO family GTPases (Fig. 1A and fig. S1A (2)). Mutations at analogous residues have been not described in other RHO or RAS proteins. Thus, the roles of Leu^{57} in GDP-GTP regulation of RHOA and in the

RHOA interaction with regulatory proteins and effectors remain to be determined. For these analyses, we utilized cell-based assays to evaluate RhoGDI binding and *Escherichia coli* (*E.coli*)-expressed recombinant proteins for in vitro biochemical analyses to evaluate intrinsic and regulated GDP-GTP cycling, and effector binding.

RhoGDI1 binds to and sequesters geranylgeranyl isoprenoid lipid modified RHOA, regulating membrane association, subcellular localization and protein stability (1, 2). Lab-generated mutations that disrupt GDP-GTP regulation (G14V and Q63L) impair RHOGDI1 association and promote enhanced RHOA association with membranes (38). Alterations that impair RHOA binding with RHOGDI1 (D45A and D185A) decrease protein stability, but increase its GTP-bound activation state (39). Therefore, we investigated if L57V alters the interaction with RhoGDI1. We ectopically expressed HA-tagged WT or mutant RHOA together with GFP-RhoGDI1 in COS-7 cells and co-immunoprecipitated HA-RHOA. As reported previously (40, 41), constitutively activated RHOA^{Q63L} and dominant-negative RHOA^{T19N} did not interact with RhoGDI1 (fig. S2, A and B) In contrast, RhoGDI1 binding to RHOA^{L57V} was comparable to RHOA^{WT}. Thus, altered association with RHOGDI1 is not a basis for the gain-of-function phenotype of RHOA^{L57V}.

The RAC1^{P29S} mutation found primarily in melanoma (42) and the atypical KRAS^{A146T} mutation in colon cancer (43) induce a gain-of-function fast cycling phenotype by enhancing intrinsic nucleotide exchange to favor formation of GTP-bound proteins. We next determined whether L57V may cause a fast-cycling alteration in RHOA. We purified *E. coli* expressed recombinant RHOA proteins and measured their intrinsic nucleotide exchange activity, utilizing mant-fluorophore labelled nucleotides in kinetic assays. We observed that RHOA^{L57V} showed an intrinsic nucleotide exchange activity comparable to that of RHOA^{WT} (Fig. 3A). We conclude that L57V does not affect intrinsic GDP-GTP cycling.

Expression of the RHOA-specific RhoGEF ECT2 is increased in gastric cancer (23) and ECT2 overexpression correlates with gastric cancer development and poor prognosis in patients (44). We showed previously that ECT2 overexpression can drive cancer growth (45–47). Therefore, we determined whether L57V may exhibit enhanced ECT2-catalyzed nucleotide exchange activity. For these analyses we utilized recombinant protein comprising the catalytic DH-PH domains of ECT2 (48). We determined that RHOA^{L57V} exhibited a similar ECT2-stimulated nucleotide exchange activity as RHOA^{WT} (RHOA^{L57V}: $k_{cat} = 24.1 \times 10^{-4}$ s^{-1}, RHOA^{WT}: $k_{cat} = 25.5 \times 10^{-4}$ s^{-1}; Fig. 3B, fig. S2C), in the same range as previously measured for ECT2 and other RhoGEFs (23, 49). Our results indicate that L57V does not alter the ability of RhoGEFs to stimulate nucleotide exchange and thus activation of RHOA.

We next determined whether L57V, like the lab-generated G14V/Q63L mutations, impairs GTP hydrolysis to favor formation of active GTP-bound RHOA. To determine the intrinsic hydrolysis of GTP to GDP, we directly detected the GTP levels bound to recombinant RHOA proteins in high performance liquid chromatography (HPLC) analyses. As shown previously (23, 50), the intrinsic GTP hydrolysis of RHOA^{Q63L} was entirely abolished (Fig. 3, C and D). RHOA^{L57V} was able to hydrolyze GTP, but significantly slower than RHOA^{WT}, indicating that the intrinsic inactivation of RHOA^{L57V} is impaired.

The lab-generated G14V/Q63L mutations also impair RhoGAP-stimulated GTP hydrolysis leading to enhanced formation of active GTP-bound RHOA. To determine if RHOA[L57V] is altered in RhoGAP sensitivity, we utilized the recombinant purified catalytic domain of the RHOA-specific RhoGAP, p190RhoGAP, expressed in gastric cancer (23) and applied a fluorophore-labelled phosphate-binding protein sensor to monitor GTP hydrolysis activity by release of the cleaved γ-phosphate. RHOA[L57V] displayed a significantly slower rate of p190RhoGAP-catalyzed GTP hydrolysis than RHOA[WT] (RHOA[L57V]: $k_{cat} = 1.9 \times 10^{-2}$ s^{-1}, RHOA[WT]: $k_{cat} = 9.4 \times 10^{-2}$ s^{-1}; Fig. 3E, fig. S2D). We conclude that L57V impairs both intrinsic and RhoGAP-catalyzed GTP hydrolysis, thereby favoring formation of active GTP-bound RHOA.

RHOA[L57V] effector interactions are not altered

We determined recently that altered association with effectors contributes to the gain-of-function phenotype of RHOA[Y42C] (23). Therefore, we next investigated if L57V also causes alterations in RHOA interaction with effectors. For these in vitro analyses, we utilized recombinant RHOA[L57V] and recombinant proteins corresponding to the isolated RHO-GTP binding domains (RBDs) of the RHOA effectors (Rhotekin, ROCK, and mDia) that mediate RHOA regulation of actin organization (51, 52). We applied fluorescence-based assays to determine WT and mutant RHOA affinities to each RBD (fig. S2E). The binding affinities that we determined for RHOA[WT] are in a similar range as reported previously to Rhotekin ($K_D = 258 \pm 15$ nM), ROCK ($K_D = 439 \pm 159$ nM) and mDia ($K_D = 310 \pm 50$ nM) (23, 53, 54). RHOA[L57V] bound with comparable affinities as RHOA[WT] to each of the effectors: Rhotekin ($K_D = 220 \pm 10$ nM), ROCK ($K_D = 243 \pm 36$ nM) and mDia ($K_D = 181 \pm 27$ nM; Fig. 3F and fig. S2E). Although recombinant RHOA[L57V] bound to the RBDs of ROCK and mDia at slightly higher affinities than WT (at 1.8- and 1.6-fold, respectively), less than 10-fold changes in affinity will not likely have substantial functional consequences on effector signaling output in vivo (12, 23). We conclude that, unlike RHOA[Y42C], RHOA[L57V] is not altered in its interaction with effectors (Fig. 3G).

Unlike RHOA[L57V], the analogous KRAS[I55V] mutant is not an activated oncogene

The DGC-associated mutational hotspot residues Leu[57] (L57) and Tyr[42] (Y42) in RHOA are also conserved in the structurally and biochemically similar RAS GTPase [Ile[55] (I55) and Tyr[40] (Y40) in RAS; fig. S1A] (16). Yet, missense *RAS* mutations in cancer are found at strikingly different positions, mainly at G12, G13 and Q61. Despite their lack of occurrence in RHOA-mutant cancer, lab-generated mutations at RHOA residues analogous to RAS G12 and Q61 result in constitutively activated gain-of-function phenotypes (31–33). Therefore, we determined if mutation of the residues in KRAS analogous to the RHOA hotspots, I55 and Y40, may still result in a gain-of-function phenotype.

For these analyses, we utilized HA1E cells, a well-characterized and widely studied human epithelial cell model for evaluation of KRAS oncogenic properties (55). Weinberg, Hahn and colleagues showed that normal human renal epithelial cells immortalized by ectopic expression of SV40 large and small T antigen and the hTERT telomerase subunit are sensitive to one-hit growth transformation by mutant KRAS. In agreement with previous analyses in rodent fibroblasts (56, 57), essentially any amino acid substitutions at RAS

G12 and Q61 resulted in a gain-of-function, as determined by the ability to cause growth transformation of HA1E cells (Fig. 3H). Similarly, 17 out of 19 substitutions at G13 also caused a gain-of-function activation of KRAS transforming potential. In contrast, when we systematically mutated the residues I55 and Y40 in KRAS to all possible amino acids, we observed that most substitutions caused a loss-, rather than gain-of-function phenotype in KRAS. Whereas RHOA[L57V] is a gain-of-function alteration, the analogous lab-generated KRAS[I55V] mutant exhibited a loss-of-function, non-oncogenic phenotype. These data provide a biological basis for the distinct mutational patterns seen with RHOA and RAS to drive cancer development despite possessing strong similarity in sequence, structure, and biochemistry.

RHOA[L57V] stimulates IGF1R and PAK1 signaling

To determine a mechanistic basis for the RHOA[L57V] gain-of-function cellular phenotypes, we applied reverse phase protein array (RPPA) to profile the signaling activation in $Cdh1^{-/-}$ gastric organoids expressing WT or mutant RHOA. Consistent with the stress fiber formation assays and our previous RPPA analyses (23), oncogenic RHOA[Y42C] increased, relative to WT, phosphorylation of cofilin at Ser[3] (fig. S3, A–C), a key downstream component of RHOA-ROCK signaling activation (58). Similarly, RHOA[L57V] also enhanced phosphorylation of cofilin, which is consistent with RHOA[L57V] stimulation of F-actin stress fibers through activation of ROCK effector signaling (Fig. 2, C and D).

The RPPA analyses showed divergence in the overall signaling expression/activity changes seen in organoids expressing RHOA[WT] or the DGC-associated L57V and Y42C mutants (fig. S3A). RHOA[L57V] but not RHOA[WT] or RHOA[Y42C] expressing organoids showed significantly increased phosphorylation of the insulin-like growth factor 1 receptor (IGF1R) tyrosine kinase at Tyr[1131] and the PAK1 serine/threonine kinase at Ser[199/204] autophosphorylation and kinase activation sites (Fig. 4, A and B). Similarly, the individual replicates of the RPPA analyses showed significantly enhanced levels of phosphorylated IGF1R (pIGF1R) and PAK1 (pPAK1) in organoids expressing RHOA[L57V], but not in those expressing RHOA[WT], RHOA[Y42C], or the empty vector (Fig. 4, C and D). Consistent with the RPPA results, immunoblot analyses in which we included additional activating phosphorylation sites verified significantly increased pIGF1R and pPAK1 levels in $Cdh1^{-/-}$ organoids expressing RHOA[L57V] but not in those expressing RHOA[WT] or the control empty vector (Fig. 4, E to G).

IGF1R phosphorylation at Tyr[1131] and Tyr[1135] (Fig. 4, E and F) activates IGF1R signaling, leading to stimulation of RHOA-dependent actin reorganization and ERK mitogen-activated protein kinase (MAPK) signaling to drive cell survival, proliferation, invasion and metastatic cancer growth (59, 60). Conversely, RHOA-induced development of stress fibers and focal adhesion complexes enhances IGF1R signaling. Similarly, phosphorylation at Ser[144], Ser[199], Ser[204] and Thr[423] induces PAK1 activity (Fig. 4, E and G) (61). PAK1 signaling has been linked to stimulation of actin dynamics and ERK MAPK signaling, that can then promote increased cell motility, survival and proliferation in cancer development (5, 62, 63).

KEGG signaling interaction network analyses of the 20 most altered RHOA[L57V]-specific proteins and phosphoproteins identified cellular processes associated with cancer growth,

cell proliferation and actin reorganization (Fig. 4, H and I). STRING-Gene Ontology-based network analyses also identified cellular processes consistent with cancer growth and cell proliferation (Fig. 4J, fig. S3D). These signaling activities are in line with our findings that RHOA^{L57V} stimulated canonical ROCK-driven actin dynamics, and additionally, promoted IGF1R and PAK1 signaling to drive cell proliferation and survival.

We conclude that RHOA^{L57V} stimulates IGF1R and PAK1 signaling, which may provide the signaling basis for the observed gain-of-function gastric organoid phenotype. This signaling mechanism is distinct from that mediated by RHOA^{Y42C}, whereby gastric oncogenesis is driven through FAK-mediated activation of PI3K-AKT and β-catenin signaling (23).

RHOA^{L57V} promotes PAK1 signaling through indirect binding to PAK1

We observed increased pPAK1 levels in RHOA^{L57V} mutant versus WT organoids (Fig. 4, A to G). To determine if this was associated with increased PAK1 signaling, we evaluated the phosphorylation levels of direct substrates of PAK1. It is well established that PAK1 phosphorylates CRAF at Ser^{338} (pCRAF) and MEK1 at Ser^{298} (pMEK1) (14) which are members of the ERK MAPK cascade regulating cell proliferation and survival (7, 8). Our RPPA analyses revealed significantly enhanced expression levels of pCRAF in RHOA^{L57V} but not in RHOA^{WT}, RHOA^{Y42C} or empty vector expressing organoids (fig. S4A). Similarly, immunoblot studies showed increased levels of pMEK1 in RHOA^{L57V} but not in RHOA^{WT} or empty vector expressing organoids (Fig. 5, A and B).

PAK1 is a canonical effector for the RHO family members RAC1, CDC42, RHOJ and RHOQ, but not RHOA (14, 64). One possible mechanism for RHOA^{L57V} activation of PAK1 may be caused by L57V alterations in RHOA structure that promote direct PAK1 binding. To address this possibility, we utilized recombinant RHOA^{WT}, RHOA^{L57V} and RAC1^{WT} and determined their ability to interact directly with the RAC/CDC42 (p21) binding domain of PAK1 expressed as recombinant GST fusion protein (PAK1-PBD). As expected, RAC1^{WT} in the active GTP analog GppNHp-bound form, but not in the inactive GDP-bound confirmation directly interacted with PAK1-PBD (fig. S4B). In line with previous observations (14, 64), RHOA^{WT} in the active or inactive form did not associate with PAK1-PBD. Similarly, GppNHp-and GDP-bound RHOA^{L57V} did not directly interact with PAK1. We conclude that RHOA^{L57V} promotes PAK1 activation and signaling through an indirect mechanism.

RHOA^{L57V} promotes YAP1 signaling

Increased RHOA activity and induction of the actin cytoskeletal network promote YAP1 signaling (65, 66), and we determined recently that RHOA^{Y42C} activates YAP1 signaling (23). Because IGF1R and PAK1 signaling have been linked with YAP1 activation (67, 68), we next determined if RHOA^{L57V}-mediated gastric oncogenesis may also involve activation of YAP1.

PAK1 inactivates the tumor suppressor Merlin by phosphorylation at Ser^{518} (68, 69) which in turn inhibits Hippo pathway MST1/2-LATS1/2-mediated phosphorylation and inactivation of YAP1. Hypophosphorylated YAP1 then translocates into the nucleus and activates YAP1-mediated gene transcription (70–72). Given that we found enhanced

levels of phosphorylated and activated PAK1 and increased phosphorylation levels of the PAK1 substrates MEK1 and CRAF in organoids expressing RHOA^{L57V}, we evaluated the expression of Ser^{518}-phosphorylated Merlin (pMerlin) by immunoblot analyses. We observed significantly increased levels of inactive pMerlin in organoids expressing RHOA^{L57V}, but not in those expressing RHOA^{WT} or the empty vector (Fig. 5, A and B).

Consistent with Merlin phosphorylation and thus its inactivation, immunoblot analyses and immunohistochemistry (IHC) staining determined that active (non-phosphorylated), nuclear YAP1 expression was enhanced in RHOA^{L57V} but not RHOA^{WT} organoids (Fig. 5, A, and C to E). Finally, verifying YAP1 activation, we evaluated the expression of established downstream targets of YAP1 in immunoblot analyses. We found increased levels of ECT2, AXL, CYR61 and Survivin (73, 74) in organoids expressing RHOA^{L57V} but not RHOA^{WT} or empty vector (Fig. 5, A and F), indicating activation of YAP1 in RHOA^{L57V} mutant organoids. Compared to WT, RHOA^{L57V} did not alter expression of total YAP1 (Fig. 5A) or the cancer-associated transcription co-factor β-catenin (Fig. 5, G and H), contrary to RHOA^{Y42C} (23). In summary, like RHOA^{Y42C}, RHOA^{L57V} promotes activation of YAP1 signaling, but through a distinct signaling mechanism.

Cdh1$^{-/-}$ organoids expressing RHOA^{L57V} are sensitive to pharmacologic inhibition of IGF1R and PAK

We next determined if RHOA^{L57V}-mediated activation of IGF1R and PAK1 signaling contributes to RHOA^{L57V}-mediated disruption of the symmetric spherical morphology in *Cdh1*-deficient gastric organoids (Fig.1, E to G). We treated the organoids with the clinical candidate IGF1R inhibitor BMS-754807 (IGF1Ri) (75) and validated target inhibition by immunoblot analyses for pIGF1R (Fig. 6A). IGF1Ri treatment reversed the abnormal morphology and the central filling seen in RHOA^{L57V} expressing organoids, as visualized by H&E staining (Fig. 6B) and phase-contrast microscopy (Fig. 6C), to the level seen in control RHOA^{WT} expressing organoids (Fig.1, E to G). Finally, IGF1Ri treatment impaired growth of RHOA^{L57V} expressing organoids (GI$_{50}$ = 179 nM, fig. S5A). The growth defect is likely at least partly due to IGF1Ri-induced apoptosis as indicated by increased levels of the apoptosis marker cleaved caspase 3 in organoids treated with IGF1Ri, but not with the vehicle DMSO (fig S5, B and C).

To assess a role for PAK1 signaling, we treated the RHOA^{L57V} expressing *Cdh1*$^{-/-}$ organoids with the group I-selective PAK inhibitor G-5555 (PAKi) (76) and validated inhibition of PAK1 activity (Fig.6A). Like IGF1Ri treatment, PAKi treatment also reversed the RHOA^{L57V}-induced abnormal organoid morphology and caused a partial collapse of their three-dimensional architecture as observed in H&E staining and phase-contrast microscopy analyses (Fig. 6, B and C). Similar to IGF1R inhibition, PAKi treatment inhibited growth of RHOA^{L57V} expressing organoids (GI$_{50}$ = 414 nM, fig. S5A) and increased expression of cleaved caspase 3 (fig. S5, B and C), suggesting that PAKi-induced apoptosis may at least partly caused the growth defect.

Concurrent inhibition of IGF1R and PAK caused the same reversion of morphology seen with each inhibitor alone (Fig. 6B), indicating that each activity alone is sufficient to drive abnormal morphology. Immunoblot analyses revealed that the combination treatment led to

a greater increase of the apoptosis marker cleaved caspase 3 than each inhibitor alone (fig. S5C). These findings support the use of pharmacologic inhibitors of IGF1R and PAK1 as a therapeutic strategy for the treatment of RHOA[L57V]-mutant gastric cancer.

DISCUSSION

Despite the conservation of RHOA residues analogous to the RAS residues that comprise cancer-associated mutational hotspots (such as G12 and Q61 in RAS), *RHOA* mutations in cancer are found at strikingly different locations in the G domain (13–16). DGC lacks effective therapies and has one of the highest *RHOA* mutation frequencies in cancer, with Y42C and L57V as the most prevalent alterations (18–20, 22). We previously identified RHOA[Y42C] as an oncogene in DGC and validated FAK as RHOA[Y42C]-specific therapeutic target for DGC (23). The L57V mutation is positioned in a structurally distinct region of the G domain. In this study, we established that, like RHOA[Y42C], RHOA[L57V] acts as a gain-of-function oncoprotein in promoting DGC. In contrast to RHOA[Y42C], which together with concurrent loss of E-cadherin caused activation of FAK (23), RHOA[L57V] expression induced activation of IGFR1 and PAK1; yet, both pathways converge on activation of YAP1 (Fig. 6D). Pharmacologic inhibition of IGFR1 and PAK1 were demonstrated in organoids as potential therapeutic approaches for RHOA[L57V]-mutant DGC.

Further supporting a gain-of-function, RHOA[L57V] exhibited the classical RHOA function of constitutively activated RHOA[Q63L], including stimulation of F-actin stress fiber formation in mouse fibroblasts. A previous study evaluating ectopic expression of WT and mutant RHOA in epithelial cells derived from mouse small intestine-derived organoids also indicated a gain-of-function phenotype for RHOA[Y42C] and RHOA[L57V] (20). They showed that mutant but not WT RHOA caused resistance to anoikis, a form of cell death caused by loss of extracellular matrix interaction (77). Resistance to anoikis is a characteristic of cancer cells and can be achieved through various signaling mechanisms that include RHO activation.

The switch I and II regions of RHOA are involved in interaction with effectors, GEFs, and GAPs. Whereas Tyr[42] is adjacent to the switch I region and core effector domain, Leu[57] lies adjacent to the switch II region and the G3 consensus guanine nucleotide binding motif. Despite their distinct locations within the RHOA G domain, RHOA[L57V] exhibited, as we observed with RHOA[Y42C] (23), impaired intrinsic and GAP-catalyzed GTP hydrolysis activities favoring formation of active GTP-bound RHOA. Consistent with its proximity to the core effector interaction domain, we determined that RHOA[Y42C] showed altered binding to effectors, with a 12-fold increased affinity for ROCK, but impaired binding to Rhotekin (23). Although the RHOA switch II region may also be involved in effector interaction (78), we determined that RHOA[L57V] binding to effectors involved actin organization was not altered. It remains possible that RHOA[L57V] exhibits altered interaction with other effectors not evaluated here that may further contribute to its distinct signaling activities. Additionally, given that IGF1R signaling is increased in gastric tumors exhibiting a mesenchymal phenotype—which includes, but is not limited to, the DGC subtype (79) —IGF1R signaling may increase the oncogenic potency of RHOA[L57V] in driving DGC tumorigenesis.

We found that RHOA^{L57V}, as we observed with RHOA^{Y42C}, promoted YAP1 activity, but through a distinct signaling mechanism (Fig. 6D). Whereas RHOA^{Y42C} activated YAP1 through FAK (23), RHOA^{L57V} activated YAP1 through PAK1-mediated inhibition of Merlin and the Hippo tumor suppressor MST1/2-LATS1/2 pathway, leading to YAP1 dephosphorylation (22, 80, 81). Both mutants may activate YAP1 through increased actin cytoskeletal organization (65–67). Because RHOA^{Y42C} and RHOA^{L57V} together comprise 42% of all *RHOA* mutations in DGC (16), activated YAP1 signaling is characteristic of a substantial percentage of RHOA-mutant DGC. Inhibitors of the TEAD transcription factors, the most common partners in YAP1-dependent gene transcription, have entered clinical evaluation (NCT04665206, NCT05228015) and may represent another therapeutic option for RHOA^{Y42C} and RHOA^{L57V} DGC. Beyond these two mutations, R5W is next most common at 11% of RHOA-mutant DGC (16). This mutation is situated in yet another very distinct region in the G domain and, consequently, is anticipated to cause mutation-selective alterations to RHOA function. Whether RHOA^{R5W} drives signaling activities that also converge on YAP1 will be interesting to determine.

Our results suggest that distinct hotspot mutations are found in RAS versus RHOA due to distinct requirements to activate their respective oncogenic potentials. This possibility is supported by our finding that mutating residues in KRAS analogous to RHOA L57V and Y42C did not activate KRAS oncogenic activity, which may explain why those *KRAS* mutations are not found in cancer. Conversely, although the lab-generated RHOA^{Q63L} mutant analogous to RAS^{Q61L} exhibits gain-of-function phenotype and potently stimulates F-actin reorganization in mouse fibroblasts, we found that *Cdh1*-intact gastric organoids tolerated expression of Y42C and L57W, but not Q63L, mutant RHOA (23). Thus, mutation of RHOA at residues analogous to RAS mutational hotspots may cause a more potent gain-of-function that is deleterious to the viability of normal gastric epithelial cells. Excessive RAS activation is also deleterious for cancer cell viability (82). Another possible contributor to the distinct hotspot mutations is DNA mutation frequencies. However, whereas virtually any of 19 possible amino acid substitutions at RAS G12 or Q61 activate RAS oncogenic potential, the cancer-associated mutational spectrum at RHOA Leu^{57} is limited to L57V (16), although four others are hypothetically possible (fig. S1B). This limited substitution profile suggests that the valine substitution uniquely endows RHOA with an altered activity that cannot be facilitated by the others. Saturation mutagenesis of RHOA Leu^{57} coupled with biochemical and cellular analyses will be needed to establish the basis for why only L57V is seen in cancer.

In summary, whereas essentially all cancer-associated RAS mutants drive cancer through sustained activation of the ERK-MAPK signaling network, RHOA^{Y42C} and RHOA^{L57V} caused hyperactivation of distinct cancer signaling networks. Extending this concept, the most prevalent RHOA mutational hotspot in all cancers is Gly^{17}, where mutations result in yet more divergent biochemical consequences, causing a dominant-negative phenotype that antagonizes RhoGEF function (16). Thus, RAS and RHOA take distinct paths to cancer, from the pattern of mutational hotspots to their consequences for GTPase function and signaling, to the broad versus narrow spectrum of cancer types where they arise.

MATERIALS AND METHODS

Constructs and cell lines

To generate N-terminal hemagglutinin (HA) epitope-tagged RHOA variants, the cDNA sequence encoding human full-length RHOA was cloned into the pCDH-HA mammalian lentivirus vector as we described previously (23). To generate RHOA fusion constructs for *E.coli* recombinant protein purification, the human *RHOA* cDNA sequence was cloned into either the pPRO-TEV-His or pGEX-4T1 bacterial expression vectors that add amino-terminal His_6 or glutathione S-transferase (GST) tags, respectively (23). Site-directed mutagenesis using the Q5 Site-directed Mutagenesis Kit (NEB) was done according to manufacturer's guidelines to generate cDNA sequences encoding RHOA mutants T19N, Y42C, L57V and Q63L. The cDNA sequences encoding the human ECT2 GEF catalytic PH-DH domain (residues 406–777) were subcloned into the pPRO-TEV-His vector and the RHO binding domain (RBD) of human ROCK1 (residues 947–101) in a pGEX4T1 vector were generated as described previously (23). The plasmid pEGFP-RhoGDI1 encoding full-length human RhoGDI1 was obtained from Mark Philips (New York University, USA) and pGEX2T1-Rhotekin-RBD (mouse, residues 7–89) from Keith Burridge (University of North Carolina at Chapel Hill, USA). The plasmids pGEX4T1-mDia1-RBD (mouse, residues 69–451) and pGEX4T1-p190RhoGAP (human, residues 1250–1531, GAP domain) were provided by Reza Ahmadian (Heinrich-Heine University, Düsseldorf, Germany). COS-7 cells (RRID:CVCL_0224) and HEK293T cells (RRID:CVCL_0063) were obtained from the American Type Culture Collection (ATCC) and NIH/3T3 mouse fibroblasts (RRID:CVCL_0594) were provided by Geoffrey Cooper (Dana-Farber Cancer Institute, Boston, MA). Cells were maintained in DMEM supplemented with 10% fetal bovine serum (HEK293T, COS-7) or Colorado calf serum (NIH/3T3), penicillin, and streptomycin. Cells were passaged for one month or 10 passages a humidified chamber with 5% CO_2 at 37°C. Cell lines were monitored regularly for mycoplasma contamination using the Lonza MycoAlert Mycoplasma Detection Kit.

Antibodies

AXL (4566, RRID:AB_2062563), β-actin (12620, RRID:AB_2797972), β-catenin (9562, RRID:AB_331149), caspase 3 (9662, RRID:AB_331439), E-cadherin (3195, RRID:AB_2291471), GFP (2956, RRID:AB_1196615), IGF1R (3027, RRID:AB_2122378), phospho-IGF1R (Y1131) (3021, RRID:AB_331578), phospho-IGF1R (Y1135) (3918, RRID:AB_10548764), MEK1/2 (4694, RRID:AB_10695868), phospho-MEK1 (S298) (9128, RRID:AB_330810), Merlin (6995, RRID:AB_10828709), phospho-Merlin (S518) (9163, RRID:AB_2149793), PAK1 (2602, RRID:AB_330222), phospho-PAK1 (S199/204) (2605, RRID:AB_2160222), phospho-PAK1 (S144) (2606, RRID:AB_2299279), phospho-PAK1 (T423) (2601, RRID:AB_330220), Survivin (2808, RRID:AB_2063948) and YAP (8418, RRID:AB_10950494) were purchased from Cell Signaling Technology. GAPDH (G8795, RRID:AB_1078991). HA (H3663, RRID:AB_262051), β-actin (A5441, RRID:AB_476744) and vinculin (V9131, RRID:AB_477629) were obtained from Sigma-Aldrich. ECT2 (07–1364, RRID:AB_10805932) was purchased from Millipore and active (non-phosphorylated) YAP (ab205270, RRID:AB_2813833) from Abcam. CYR61 (sc-374129, RRID:AB_10947399) and RHOA (sc-418, RRID:AB_628218) were

obtained from Santa Cruz Biotechnology. Anti-mouse IgG HRP-linked antibody (7076, RRID:AB_330924) and anti-rabbit IgG HRP-linked antibody (7074, RRID:AB_2099233) were purchased from Cell Signaling Technology. Phalloidin conjugated with an Alexa-488 fluorophore (A12379) and DAPI (D3571) were obtained from Invitrogen. Antibodies used in the RPPA analysis are listed in data file S1.

Isolation, culturing and drugging of mouse gastric organoids

Mist1-CreERT2, *Cdh1*$^{Flox/Flox}$ *R26*-mTmG mice were described previously (23) and maintained and used accordingly the guidelines of the Institutional Animal Care and Use Committee of the Dana- Farber Cancer Institute (Boston, MA). Detailed methods for the generation of mouse-derived gastric organoids were described previously (23). Briefly, the stomach was harvested upon humane sacrifice of *Mist1*-CreERT2, *Cdh1*$^{Flox/Flox}$ *R26*-mTmG mice, opened longitudinally and the gastric contents were removed. The tissue was washed with ice-cold PBS in a 90 mm dish, washed with 20 ml ice-cold PBS in a 50 ml tube under vigorous shaking, and rinsed with ice-cold PBS in a dish. The tissue was transferred to a 35 mm petri dish and minced with fine scissors. Tissue fragments were incubated with 1 ml collagenase (Invitrogen) at 37°C under vigorous mixing every 5–10 min using a 1,000 µl pipette. Single epithelial units (crypts/pits) were separated from larger tissue fragments using a phase or dissection microscope. The epithelial units were filtrated through a 70 µm cell strainer (BD), followed by washing with 9 ml washing media (penicillin (100 units/ml), streptomycin (0.1 mg/ml), L-glutamine (2 mM), and FBS (10%) in DMEM/F12 (Invitrogen) with HEPES). The filtrate was transferred into a 15 ml tube and centrifuged at 200 g for 5 min. After resuspending the pellet in 0.5–1 ml washing medium, it was transferred to a new 1.5 ml tube, centrifuged at 200 g for 5 min and stored on ice. The epithelial units were resuspended in 15 µl Matrigel (Corning) per well. Fifteen µl of the cell-Matrigel suspension was transferred in the center of a well in a 24-well-plate and spread with a pipette tip. During polymerization of the Matrigel, plates were incubated upside down to avoid the epithelial units from attaching to the plate surface. Plates were returned to the upright orientation after 3–5 min and 500 µl of 50% L-WRN conditioned medium (83), a 1:1 mix of L-WRN conditioned medium and Advanced DMEM/F-12 with 20% FBS, were added per well. Medium was refreshed every 48 hours. Organoids were cultured at 37°C and 5% CO_2. For organoid up-culturing, 6-well-plates with 7 aliquots cell-Matrigel suspension in 2.5 ml conditioned medium per well were used instead of 24-well-plates with one aliquot in 500 µl conditioned medium per well. To deplete *Cdh1*, organoids were incubated with 2 µM tamoxifen (TAM) for 48 hours at 37°C and 5% CO_2. *Cdh1*$^{-/-}$ organoids were then infected with lentivirus encoding HA-tagged RHOA variants or control empty vector (see below). *Cdh1*$^{-/-}$ organoids stably expressing RHOA^{L57V} were treated with DMSO, the IGFR1 inhibitor BMS-754807 (200 nM), PAK inhibitor G5555 (200 nM) or the distinct combination (each 200 nM) for 48 hours (H&E staining, phase-contrast images) or 24 hours (immunoblotting) at 37°C and 5% CO_2.

Lentiviral infection of organoids and cell lines

For organoid infection, *Cdh1*$^{-/-}$ organoids in 50% L-WRN conditioned media were transferred into a 15 ml tube, centrifuged at 200 x g for 5 min, resuspended in 200 µl trypsin-EDTA, and incubated at 37°C for 5 min. After adding 1 ml washing media (see

above), organoids were dissociated by vigorous pipetting and centrifuged at 200 g for 5 min. Organoids were resuspended in 250 μl of a solution containing lentivirus, encoding the HA-RHOA variants, 8 μg/ml polybrene and 10 μM Y27632 (R&D). Lentivirus was generated as described previously (84). Each condition of the lentivirus-organoid suspension was transferred to a single well of a 48-well-plate, sealed with Parafilm (Bemis Co.) and centrifuged at 600 g at 32°C for 1 hour. Plates were incubated for 6 hours at 37°C. Organoids were then resuspended in 1 ml conditioned organoid media per well, transferred to a 1.5 ml tube and centrifuged at 200 g for 5 min. Organoids were resuspended in 20 μl Matrigel and cultured as described above, except that the medium contained puromycin for 7 days to select for infected cells. For infection of NIH/3T3 fibroblasts, lentivirus was generated as described previously (23). Briefly, 0.9×10^6 HEK293T cells were seeded in a T25 flask. The next day, 500 μl OptiMEM were incubated with 25 μl Fugene 6 (Promega), 3 μg psPax, 1 μg pMD2.G, and 4 μg pCDH-HA-RHOA variant for 15 min accordingly manufacture's guidelines and added to the flasks. After overnight incubation, the media was changed to DMEM supplemented with 20% FBS. After additional 48 hours, the viral supernatant was filtrated through a 0.45 μm PES syringe filter (Nalgene) and stored at −80°C. In a T25 flask, 10^5 NIH/3T3 cells were infected with 2ml complete culture medium with 8 μg/ml polybrene, and 500 μl lentivirus. After 8 hours, medium was replaced through complete culture media. After 24 hours, infected cells were selected with media supplemented with 2 μg/ml puromycin for 48–72 hours.

Organoid viability assays

Organoids were dissociated using TrypLE Express (Thermo Fisher) and cells were seeded into ultra-low attachment 384-well plates (Corning) at 1000 viable cells per well into 20μl of culture media, consisting of 10% Matrigel (Corning) and 90% organoid medium. After 24 hours, organoids were treated with increasing concentrations (0.0001–10 μM) of the IFG1R inhibitor BMS-754807 (Selleck Chemicals), PAK inhibitor G-5555 (Selleck Chemicals) or DMSO as control in a randomized fashion using a Tecan D300e Digital Dispenser (Tecan Trading). Cell viability was measured six days post-treatment using the Cell-TiterGlo 3D Cell Viability assay kit (Promega) according to the manufacturer's instructions. Fluorescence signals were detected using a FLUOstar Omega microplate reader. Technical triplicates were conducted for each biological replicate with three biological replicates for each organoid variant. The calculation of the half maximal inhibitory concentration (GI_{50}) was conducted in R (v.4.2.1) with the R package dr4p.

Immunoblot analyses

NIH/3T3 fibroblasts were washed twice with ice-cold PBS and incubated in lysis buffer (25 mM Tris-HCl, pH 7.4, 100 mM NaCl, 10 mM $MgCl_2$, 1% NP-40) supplemented with protease (Roche) and phosphatase (Sigma-Aldrich) inhibitors for 10 min on ice. Cells were scraped and lysates were collected and centrifuged at 15,000 *g* for 15 min at 4°C. The cleared lysates were transferred into a new tube. Protein concentrations were determined using Bradford reagent (Bio-Rad). Equal protein amounts per sample were loaded into gels and standard immunoblotting procedures were performed. Organoids were grown for 3–5 days, collected and dissociated using TrypLE Express. Dissociated cells were seeded at a density of 40,000 cells per 25μl Matrigel; 7 Matrigel aliquots in 2.5 ml 50% L-WRN

conditioned medium per well of a 6-well plate. The Matrigel around the organoids was removed using Cell Recovery Solution (Corning). The released organoids were pelleted by centrifugation and lysed for immunoblotting as previously described (23).

Histological and immunohistochemical staining of organoids

Organoids were fixed in 10% formalin overnight, resuspended in bacto-agar and embedded in paraffin. Standard protocols for H&E or alcian blue staining were used as described previously (23). For IHC staining of active YAP or β-catenin, slide deparaffinization was performed accordingly standard protocol (23). Briefly, 250 ml of citric acid buffer was placed into a slide container filled with up to 12 slides. The solution was warmed to 100°C for 10 min, cooled for 5 min, warmed for 2 min, cooled for 5 min, warmed for 2 min, then cooled down to RT. Buffer was replaced with PBS to wash the slides, utilizing a rocker. The slides were incubated in 10% H_2O_2 for 15 min at RT and washed 3 times with PBS. The slides were placed in a slide box and the cells were circled using an oil pen. After blocking with BSA (Sigma) for 20 min at RT, primary antibody was incubated overnight at 4°C. The slides were washed three times with PBS, incubated with secondary antibody (anti-rabbit serum, 1:200 in PBS) for 50 min at RT, stained with DAB (1:100), washed with H_2O, stained with hematoxylin, and mounted using standard protocol. For quantitation, positively stained cells of three random views were counted and then divided by the total cells per area organoids, using FIJI.

Stress fiber formation assays

NIH/3T3 cells expressing pCDH-RHOA variants were seeded on 10 μg/ml fibronectin-coated glass coverslips. When 80% confluency was reached, cells were washed twice with PBS, fixed in 3.7% formaldehyde (Fisher Scientific) for 10 min at RT, washed with PBS and permeabilized with 0.1% Triton-X100 (Sigma) for 5 min at RT. After blocking with 2% BSA (Sigma) in PBS for 30 min at RT, cells were incubated with phalloidin conjugated with an Alexa-488 fluorophore (Invitrogen) diluted in 2% BSA-PBS for 45 min at RT. Cells were washed three times with PBS. To visualize the nucleus, cells were then stained with DAPI (1:10,000) for 10 min in PBS and then washed twice with PBS. Cells were mounted with ProLong Diamond Antifade Mountant (Invitrogen). For each condition, 10 random views were acquired on an Olympus FV1000 confocal microscope using a 40x objective. To determine F-actin stress fiber formation, the corrected total cell fluorescence intensity of the phalloidin signal of each cell, corrected for cell size and background was determined as described previously (23), using FIJI or cell profiler. The corrected total cell fluorescence was calculated as integrated density of the cell/(cell area x mean fluorescence of background readings).

Cell adhesion assays

NIH/3T3 mouse fibroblast cell lines stably expressing exogenous HA-RHOA variants were plated in 96-well plates were coated with 10 μg/ml fibronectin that were blocked with 1% BSA/PBS for 30 min at RT. After 24 hours, the cultures were then incubated with 2 μM CellTracker CMFDA (5-chloromethylfluorescein diacetate) for 10 min at 37°C, added to wells (2.5×10^4 cells per well) in triplicate, allowed to adhere for 1 hour, and washed

with PBS. The fluorescence signal was determined using a SpectraMax i3x plate reader (Molecular Devices, excitation at 485 nm and emission at 535 nm).

Cell migration assays

One day before the experiment, 5×10^3 NIH/3T3 cells expressing HA-RHOA were seeded in a 10 μg/ml fibronectin-coated 60 mm glass bottom dish (MatTEK Corporation). The next day, live-cell imaging was performed using a 10x objective on an Olympus Viva View FL Incubator time-lapse microscope equipped with a Hamamatsu Orca R2 cooled charge-coupled device (CCD) camera and Metamorph software. Differential interference contrast (DIC) images were collected every 10 min for 16 h at 37°C and 5% CO_2, Cells were tracked, and velocities were calculated using ImageJ. Only single cells were tracked. NIH/3T3 cells were excluded after a collision event with another cell or debris, or after division, death or migration out of the field of view.

Recombinant protein expression and purification

RHOA proteins, p190RhoGAP domain, ECT2-PH-DH domain, ROCK-RBD, mDia-RBD and Rhotekin-RBD were expressed in *E. coli* BL21 (DE3) Rosetta2 cells in Terrific Broth (TB) medium by overnight expression at 18°C following induction with 250 μM isopropyl-β-D-1-thiogalactopyranoside at an OD_{600} of around 0.6 at 37°C, as previously described (23). ROCK-RBD, mDia-RBD, Rhotekin-RBD and p190RhoGAP were purified as GST-fusion proteins at 4°C using glutathione sepharose 4B chromatography (GE Life Sciences) accordingly manufacture's guidelines, followed by cleavage of the GST-tag (only for p190RhoGAP) and Superdex75 size exclusion chromatography (GE Life Sciences) as previously described (23). ECT2 was purified as a His-fusion protein at 4°C using HisTRAP nickel Sepharose chromatography (GE Life Sciences) accordingly standard protocols, followed by cleavage of the His-tag and size exclusion chromatography (23). RHOA proteins were purified either as GST- or His-tagged protein, followed by tag cleavage and size exclusion chromatography. Fractions were analyzed by SDS-PAGE, fractions with greater than 90% purity were pooled, aliquoted, flash frozen in liquid nitrogen and stored at −80°C. Proteins were stored in 50 mM HEPES pH 7.5, 150 mM NaCl, 5% glycerol and 5 mM β-mercaptoethanol. Buffer for RHOA contained in addition 5 mM $MgCl_2$.

Nucleotide exchange

Recombinant RHOA proteins or $RAC1^{WT}$ (RC-01, Cytoskeleton) were loaded with 2'-/3'-O-(N'-methylanthraniloyl) guanosine-5'-O-diphosphate (mantGDP; Jena Biosciences), guanosine-5'-triphosphate (GTP, Sigma) or guanosine-5'-[(β,γ)-imido]triphosphate (GppNHp, Sigma) with 10-fold (mantGDP) or 40-fold (GTP, GppNHp) molar nucleotide excess, 20 mM EDTA and 200 mM $(NH_4)_2SO_4$ in 50 mM HEPES pH 7.5, 100 mM NaCl and 5 mM β-mercaptoethanol. After overnight incubation at 4°C, 125 mM $MgCl_2$ was added for 10 min on ice. Unbound nucleotide was removed by a NAP-5 size exclusion chromatography column (GE Life Sciences) equilibrated in 50 mM HEPES pH 7.5, 100 mM NaCl, 5 mM $MgCl_2$, 5% glycerol and 5 mM β-mercaptoethanol. RHOA was loaded with 2'/3'-O-(N-Methyl-anthraniloyl)-guanosine-5'-[(β,γ)-imido]triphosphate (mantGppNHp, Jena Bioscience) with 1.5-fold molar excess of mantGppNHp, 60 mM $(NH_4)_2SO_4$, 0.3 mM $ZnCl_2$ and alkaline phosphatase conjugated to Sepharose beads at

10% (vol/vol) in 50 mM HEPES pH 7.5, 100 mM NaCl and 5 mM β-mercaptoethanol. After head-over-head rotation at 4°C for 2 days, phosphatase and unbound nucleotide were removed by a NAP-5 column. RHOA-containing fractions were pooled, and protein concentration via absorption at 280 nm and nucleotide loading efficiency via HPLC were measured. RHOA-mantGDP or -mantGppNHp were frozen in liquid nitrogen and stored at −80°C. RHOA-GTP was immediately used in experiments.

Guanine nucleotide exchange assays

Experiments were performed with 0.4 μM RHOA-mantGDP and, when indicated, with different RhoGEF ECT2 concentrations, in 25 mM HEPES pH 7.5, 50 mM NaCl, 5 mM $MgCl_2$, 5% glycerol and 5 mM β-mercaptoethanol. Mant-nucleotide dissociation was initiated by adding 1 mM GDP (Sigma, 2,500-fold excess). Fluorescence signal (excitation at 360 nm, emission at 439 nm) was detected every 15 seconds at 25°C in a Cary Eclipse Fluorescence Spectrophotometer (Agilent). The dissociation rate (observed rate k_{obs}) was determined by utilizing a mono-exponential decay equation in GraphPad Prism. The k_{cat} of ECT2 activity was determined by fitting k_{obs} rates against the ECT2 concentrations.

HPLC intrinsic GTP hydrolysis assays

Assays were performed with 70 μM RHOA-GTP in 50 mM HEPES pH 7.5, 100 mM NaCl, 5 mM $MgCl_2$, 5% glycerol and 5 mM β-mercaptoethanol at 25°C. Aliquots of 40 μl were flash frozen in liquid nitrogen at indicated time points. After 2 min at 95°C, samples were centrifuged at 14,000 g for 1 min at RT and the supernatant was applied to a high-performance liquid chromatography column (HPLC, Agilent 1100). GDP and GTP were separated on a C18-column (Agilent) with 100 mM potassium-phosphate pH 6.5, 10 mM tert-butyl-ammonium-bromide and 7.5% acetonitrile as described previously (23). The concentration of non-hydrolyzed GTP was plotted against time and data were described by a mono-exponential equation to determine the observed rate constant (k_{obs}) using GraphPad Prism. The efficiency of RHOA nucleotide loading was measured in a similar way (25% acetonitrile for mant-nucleotides).

GAP-stimulated GTP hydrolysis assays using a phosphate sensor

Cuvettes and stirrers were incubated with 200 μM 7-methyl guanosine and 1 U/ml purine nucleoside phosphorylase for 30 min at RT to reduce phosphate contamination. Assays were performed as previously described (23, 85). Briefly, 2 μM RHOA-GTP were incubated with indicated p190RhoGAP concentrations in the presence of 5 μM of MDCC-labelled phosphate-binding protein (MDCC-PBP, Thermo Fisher Scientific) in 50 mM HEPES pH 7.5, 100 mM NaCl, 5 mM $MgCl_2$, and 2 mM dithiothreitol. The increase in MDCC-fluorescence (excitation: 430 nm, emission: 460 nm) due to the phosphate release of the GTP hydrolysis was detected at 25°C in a Cary Eclipse Fluorescence Spectrophotometer. The observed rate (k_{obs}) was determined by describing the reaction with a mono-exponential equation in GraphPad Prism. The k_{cat} of p190RhoGAP activity was calculated by fitting the k_{obs} values against the GAP concentrations.

Effector-nucleotide dissociation studies

RHOA binding to effectors was determined by measuring inhibition of mant-nucleotide dissociation from RHOA due to effector binding, as described previously (23). Experiments were performed with 0.6 μM RHOA-mantGppNHp and indicated concentrations of Rhotekin-RBD, ROCK1-RBD or mDia1-RBD in 50 mM HEPES pH 7.5, 100 mM NaCl, 5 mM $MgCl_2$, 5% glycerol and 5 mM β-mercaptoethanol. Mant-nucleotide dissociation was initiated by adding 600 μM GppNHp (Sigma; 1,000-fold excess). Fluorescence signal (excitation: 360 nm, emission: 439 nm) was detected at 25°C in a Cary Eclipse Fluorescence Spectrophotometer. Nucleotide dissociation rate (k_{obs}) was determined by utilizing a mono-exponential decay equation. The k_{obs} values were fitted against the effector concentration to calculate the binding affinity K_D.

RhoGDI co-immunoprecipitation assays

COS-7 cells were transiently co-transfected with indicated pCDH-HA-RHOA variant and pEGFP-RHOGDI1 and lysed on ice in lysis buffer (1% Triton X-100, 150 mM NaCl, 50 mM Tris-HCl, pH 7.4, 10 mM $MgCl_2$) supplemented with protease (Roche) and phosphatase (Sigma-Aldrich) inhibitors. Samples were centrifuged at 14,000 g for 10 min at 4°C. Equal amount of protein was incubated with anti-HA epitope-conjugated agarose beads (Sigma) for 2 hours at 4°C with head-over-head rotation. Beads were washed five times in lysis buffer (with 250 mM NaCl) and boiled in 2x SDS sample buffer (0.25 M Tris-HCl pH 6.8, 8% SDS (w/v), 40% glycerol (w/v), 10% β-mercaptoethanol (w/v) and 0.2% bromophenol blue (w/v)).

Pull-down studies to determine direct binding to PAK1

GSH-beads coupled to GST-PAK1-PBD (PAK02, Cytoskeleton) which were three times washed with 50 mM HEPES pH 7.5, 100 mM NaCl, 5 mM $MgCl_2$ and 5 mM β-mercaptoethanol. Experiments were performed with 60 μg (60 μl) GST-PAK1-PBD bound to GSH beads and 30 μg RHO^{WT}, $RHOA^{L57V}$ or $RAC1^{WT}$ bound either to GppNHp or GDP in 50 mM HEPES pH 7.5, 100 mM NaCl, 5 mM $MgCl_2$, 5 mM β-mercaptoethanol and 100 μM GppNHp or GDP for one hour at 4°C with head-over-head rotation. Beads were washed three times with 50 mM HEPES pH 7.5, 100 mM NaCl, 5 mM $MgCl_2$ and 5 mM β-mercaptoethanol and boiled in 30 μl 4x Laemmli sample buffer (Bio-Rad Laboratories) supplemented with β-mercaptoethanol. Samples were analyzed utilizing immunoblotting on nitrocellulose membranes (Millipore) followed by staining with Ponceau S solution (Thermo Fisher Scientific).

Mutational KRAS screening studies

Data were retrieved from reference (86) and are available online at https://www.targetkras.com/. Briefly, SV40 large and small T and telomerase (hTERT)-immortalized human embryonic kidney (HA1E) cells (55) (RRID:CVCL_VU89) expressing a screening library of indicated KRAS mutations were evaluated for their transforming activity as previously described (86). After 7 days, cells were harvested and sequenced. Relative allele abundance is shown as a Log_2 fold change comparing the ultra-low attachment and the high attachment conditions.

Reverse phase protein array (RPPA) studies

RPPA experiments were performed with four biological replicates using $Cdh1^{-/-}$ gastric organoids expressing indicated HA-RHOA variants or empty vector. Samples were prepared as described previously (87). Organoid lysates were immobilized onto nitrocellulose-coated glass slides (Grace Bio-labs) in three technical replicates using an Aushon 2470 arrayer (Quanterix), together with reference standards for internal quality control. Arrays were pre-treated with Reblot Antibody Stripping solution (MilliporeSigma) for 15 min at RT, followed by two PBS washes and incubated for 5 hours in I-block (Invitrogen) before antibody staining. Samples were then stained using an automated system (Agilent DakoCytomation) as previously described (87) and arrays were probed with 120 antibodies (data file S1) targeting unmodified and phosphorylated residues of pre-selected signaling proteins. Antibodies used for the RPPA were validated for their specificity against their target as previously described (88). Selected arrays were stained with Sypro Ruby Protein Blot Stain (Invitrogen) following manufacturer's recommendations to quantify the amount of protein in each sample (87) and used for normalization purposes. Sypro Ruby and antibody-stained slides were scanned on a Tecan laser scanner (TECAN) and images were analyzed using the commercially available software MicroVigene Version 5.1.0.0 (Vigenetech) as previously described (89). For computational analyses, antibody intensity values were imported into R (version 3.5.2) and supervised hierarchical clustering was performed. Heatmaps were generated using the ComplexHeatmap package (Bioconductor). The RPPA standardized intensity data were log2 transformed, and the median of four biological replicates was determined for each condition. Testing between specific comparisons utilized the Student's t-test or one-way ANOVA with P-values < 0.05 denoting significant alterations and results were represented by volcano plots. P-values were corrected using the Benjamini-Hochberg correction. Top 20 hits of the volcano plot comparing RHOA^{L57V} with RHOA^{WT} were characterized in KEGG signaling pathway and Gene Ontology analyses utilizing the STRING protein-protein interaction networks functional enrichment analysis database (90). The signaling network of those top 20 hits was determined using STRING with a minimum interaction score of 0.7 (high confidence). The interaction network was visualized using Gephi software to calculate the modularity and plot the genes in a radial axis layout arranged by their modularity and color-coded to their $\log_2$ fold change score (91).

Statistical analyses

Data are represented as mean $\pm$ S.E.M for n 3 independent experiments (except where noted). For each experiment, the number of independent biological experiments are noted in the figure legends, with representative images shown of replicates with similar results. Statistical analysis was performed in GraphPad Prism using an unpaired two-tailed Student's t-test, one-way ANOVA with Dunnett's multiple comparison or Benjamini-Hochberg correction or Mann-Whitney test as indicated in the figure legends. P-values are denoted by $*P < 0.05$, $**P < 0.01$, $*** P < 0.001$, $****P < 0.0001$, ns, not significant.

Supplementary Material

Refer to Web version on PubMed Central for supplementary material.

Acknowledgements:

Data and materials availability:

All data needed to evaluate the conclusions in the paper are present in the paper or the Supplementary Materials. Materials are available upon request from the corresponding authors.

REFERENCES AND NOTES

1. Hodge RG, Ridley AJ, Regulating Rho GTPases and their regulators. Nat Rev Mol Cell Biol 17, 496–510 (2016). [PubMed: 27301673]

2. Hodge RG, Schaefer A, Howard SV, Der CJ, RAS and RHO family GTPase mutations in cancer: twin sons of different mothers? Crit Rev Biochem Mol Biol 55, 386–407 (2020). [PubMed: 32838579]

3. Simanshu DK, Nissley DV, McCormick F, RAS Proteins and Their Regulators in Human Disease. Cell 170, 17–33 (2017). [PubMed: 28666118]

4. Hobbs GA, Der CJ, Rossman KL, RAS isoforms and mutations in cancer at a glance. J Cell Sci 129, 1287–1292 (2016). [PubMed: 26985062]

5. Crosas-Molist E, Samain R, Kohlhammer L, Orgaz JL, George SL, Maiques O, Barcelo J, Sanz-Moreno V, Rho GTPase signaling in cancer progression and dissemination. Physiol Rev 102, 455–510 (2022). [PubMed: 34541899]

6. Lawson CD, Ridley AJ, Rho GTPase signaling complexes in cell migration and invasion. J Cell Biol 217, 447–457 (2018). [PubMed: 29233866]

7. Cox AD, Der CJ, Ras history: The saga continues. Small GTPases 1, 2–27 (2010). [PubMed: 21686117]

8. Johnson C, Burkhart DL, Haigis KM, Classification of KRAS-Activating Mutations and the Implications for Therapeutic Intervention. Cancer Discov 12, 913–923 (2022). [PubMed: 35373279]

9. Prior IA, Hood FE, Hartley JL, The Frequency of Ras Mutations in Cancer. Cancer Res 80, 2969–2974 (2020). [PubMed: 32209560]

10. Cook JH, Melloni GEM, Gulhan DC, Park PJ, Haigis KM, The origins and genetic interactions of KRAS mutations are allele- and tissue-specific. Nat Commun 12, 1808 (2021). [PubMed: 33753749]

11. Hobbs GA, Baker NM, Miermont AM, Thurman RD, Pierobon M, Tran TH, Anderson AO, Waters AM, Diehl JN, Papke B, Hodge RG, Klomp JE, Goodwin CM, DeLiberty JM, Wang J, Ng RWS, Gautam P, Bryant KL, Esposito D, Campbell SL, Petricoin EF 3rd, Simanshu DK, Aguirre AJ, Wolpin BM, Wennerberg K, Rudloff U, Cox AD, Der CJ, Atypical KRAS(G12R) Mutant Is Impaired in PI3K Signaling and Macropinocytosis in Pancreatic Cancer. Cancer Discov 10, 104–123 (2020). [PubMed: 31649109]

12. Huynh MV, Hobbs GA, Schaefer A, Pierobon M, Carey LM, Diehl JN, DeLiberty JM, Thurman RD, Cooke AR, Goodwin CM, Cook JH, Lin L, Waters AM, Rashid NU, Petricoin EF 3rd, Campbell SL, Haigis KM, Simeone DM, Lyssiotis CA, Cox AD, Der CJ, Functional and biological heterogeneity of KRAS(Q61) mutations. Sci Signal 15, eabn2694 (2022). [PubMed: 35944066]

13. Bustelo XR, RHO GTPases in cancer: known facts, open questions, and therapeutic challenges. Biochem Soc Trans 46, 741–760 (2018). [PubMed: 29871878]

14. Cannon AC, Uribe-Alvarez C, Chernoff J, RAC1 as a Therapeutic Target in Malignant Melanoma. Trends Cancer 6, 478–488 (2020). [PubMed: 32460002]

15. Porter AP, Papaioannou A, Malliri A, Deregulation of Rho GTPases in cancer. Small GTPases 7, 123–138 (2016). [PubMed: 27104658]

16. Schaefer A, Der CJ, RHOA takes the RHOad less traveled to cancer. Trends Cancer 8, 655–669 (2022). [PubMed: 35568648]

17. Sung H, Ferlay J, Siegel RL, Laversanne M, Soerjomataram I, Jemal A, Bray F, Global Cancer Statistics 2020: GLOBOCAN Estimates of Incidence and Mortality Worldwide for 36 Cancers in 185 Countries. CA Cancer J Clin 71, 209–249 (2021). [PubMed: 33538338]

18. Kakiuchi M, Nishizawa T, Ueda H, Gotoh K, Tanaka A, Hayashi A, Yamamoto S, Tatsuno K, Katoh H, Watanabe Y, Ichimura T, Ushiku T, Funahashi S, Tateishi K, Wada I, Shimizu N, Nomura S, Koike K, Seto Y, Fukayama M, Aburatani H, Ishikawa S, Recurrent gain-of-function mutations of RHOA in diffuse-type gastric carcinoma. Nat Genet 46, 583–587 (2014). [PubMed: 24816255]

19. Cancer T Genome Atlas Research Network, Comprehensive molecular characterization of gastric adenocarcinoma. Nature 513, 202–209 (2014). [PubMed: 25079317]

20. Wang K, Yuen ST, Xu J, Lee SP, Yan HH, Shi ST, Siu HC, Deng S, Chu KM, Law S, Chan KH, Chan AS, Tsui WY, Ho SL, Chan AK, Man JL, Foglizzo V, Ng MK, Chan AS, Ching YP, Cheng GH, Xie T, Fernandez J, Li VS, Clevers H, Rejto PA, Mao M, Leung SY, Whole-genome sequencing and comprehensive molecular profiling identify new driver mutations in gastric cancer. Nat Genet 46, 573–582 (2014). [PubMed: 24816253]

21. Kourtidis A, Lu R, Pence LJ, Anastasiadis PZ, A central role for cadherin signaling in cancer. Exp Cell Res 358, 78–85 (2017). [PubMed: 28412244]

22. Mun DG, Bhin J, Kim S, Kim H, Jung JH, Jung Y, Jang YE, Park JM, Kim H, Jung Y, Lee H, Bae J, Back S, Kim SJ, Kim J, Park H, Li H, Hwang KB, Park YS, Yook JH, Kim BS, Kwon SY, Ryu SW, Park DY, Jeon TY, Kim DH, Lee JH, Han SU, Song KS, Park D, Park JW, Rodriguez H, Kim J, Lee H, Kim KP, Yang EG, Kim HK, Paek E, Lee S, Lee SW, Hwang D, Proteogenomic

Characterization of Human Early-Onset Gastric Cancer. Cancer Cell 35, 111–124 e110 (2019). [PubMed: 30645970]

23. Zhang H, Schaefer A, Wang Y, Hodge RG, Blake DR, Diehl JN, Papageorge AG, Stachler MD, Liao J, Zhou J, Wu Z, Akarca FG, de Klerk LK, Derks S, Pierobon M, Hoadley KA, Wang TC, Church G, Wong KK, Petricoin EF, Cox AD, Lowy DR, Der CJ, Bass AJ, Gain-of-Function RHOA Mutations Promote Focal Adhesion Kinase Activation and Dependency in Diffuse Gastric Cancer. Cancer Discov 10, 288–305 (2020). [PubMed: 31771969]

24. Kumagai S, Togashi Y, Sakai C, Kawazoe A, Kawazu M, Ueno T, Sato E, Kuwata T, Kinoshita T, Yamamoto M, Nomura S, Tsukamoto T, Mano H, Shitara K, Nishikawa H, An Oncogenic Alteration Creates a Microenvironment that Promotes Tumor Progression by Conferring a Metabolic Advantage to Regulatory T Cells. Immunity 53, 187–203 e188 (2020). [PubMed: 32640259]

25. Hayakawa Y, Ariyama H, Stancikova J, Sakitani K, Asfaha S, Renz BW, Dubeykovskaya ZA, Shibata W, Wang H, Westphalen CB, Chen X, Takemoto Y, Kim W, Khurana SS, Tailor Y, Nagar K, Tomita H, Hara A, Sepulveda AR, Setlik W, Gershon MD, Saha S, Ding L, Shen Z, Fox JG, Friedman RA, Konieczny SF, Worthley DL, Korinek V, Wang TC, Mist1 Expressing Gastric Stem Cells Maintain the Normal and Neoplastic Gastric Epithelium and Are Supported by a Perivascular Stem Cell Niche. Cancer Cell 28, 800–814 (2015). [PubMed: 26585400]

26. Nam KT, Lee HJ, Sousa JF, Weis VG, O'Neal RL, Finke PE, Romero-Gallo J, Shi G, Mills JC, Peek RM Jr., Konieczny SF, Goldenring JR, Mature chief cells are cryptic progenitors for metaplasia in the stomach. Gastroenterology 139, 2028–2037 e2029 (2010). [PubMed: 20854822]

27. Stange DE, Koo BK, Huch M, Sibbel G, Basak O, Lyubimova A, Kujala P, Bartfeld S, Koster J, Geahlen JH, Peters PJ, van Es JH, van de Wetering M, Mills JC, Clevers H, Differentiated Troy+ chief cells act as reserve stem cells to generate all lineages of the stomach epithelium. Cell 155, 357–368 (2013). [PubMed: 24120136]

28. Nanki K, Toshimitsu K, Takano A, Fujii M, Shimokawa M, Ohta Y, Matano M, Seino T, Nishikori S, Ishikawa K, Kawasaki K, Togasaki K, Takahashi S, Sukawa Y, Ishida H, Sugimoto S, Kawakubo H, Kim J, Kitagawa Y, Sekine S, Koo BK, Kanai T, Sato T, Divergent Routes toward Wnt and R-spondin Niche Independency during Human Gastric Carcinogenesis. Cell 174, 856–869 e817 (2018). [PubMed: 30096312]

29. Yan HHN, Siu HC, Law S, Ho SL, Yue SSK, Tsui WY, Chan D, Chan AS, Ma S, Lam KO, Bartfeld S, Man AHY, Lee BCH, Chan ASY, Wong JWH, Cheng PSW, Chan AKW, Zhang J, Shi J, Fan X, Kwong DLW, Mak TW, Yuen ST, Clevers H, Leung SY, A Comprehensive Human Gastric Cancer Organoid Biobank Captures Tumor Subtype Heterogeneity and Enables Therapeutic Screening. Cell Stem Cell 23, 882–897 e811 (2018). [PubMed: 30344100]

30. Hu B, El Hajj N, Sittler S, Lammert N, Barnes R, Meloni-Ehrig A, Gastric cancer: Classification, histology and application of molecular pathology. J Gastrointest Oncol 3, 251–261 (2012). [PubMed: 22943016]

31. Paterson HF, Self AJ, Garrett MD, Just I, Aktories K, Hall A, Microinjection of recombinant p21rho induces rapid changes in cell morphology. J Cell Biol 111, 1001–1007 (1990). [PubMed: 2118140]

32. Ridley AJ, Microinjection of Rho and Rac into quiescent Swiss 3T3 cells. Methods Enzymol 256, 313–320 (1995). [PubMed: 7476447]

33. Ridley AJ, Hall A, The small GTP-binding protein rho regulates the assembly of focal adhesions and actin stress fibers in response to growth factors. Cell 70, 389–399 (1992). [PubMed: 1643657]

34. Khosravi-Far R, Chrzanowska-Wodnicka M, Solski PA, Eva A, Burridge K, Der CJ, Dbl and Vav mediate transformation via mitogen-activated protein kinase pathways that are distinct from those activated by oncogenic Ras. Mol Cell Biol 14, 6848–6857 (1994). [PubMed: 7935402]

35. Warner H, Wilson BJ, Caswell PT, Control of adhesion and protrusion in cell migration by Rho GTPases. Curr Opin Cell Biol 56, 64–70 (2019). [PubMed: 30292078]

36. Olivo C, Vanni C, Mancini P, Silengo L, Torrisi MR, Tarone G, Defilippi P, Eva A, Distinct involvement of cdc42 and RhoA GTPases in actin organization and cell shape in untransformed and Dbl oncogene transformed NIH3T3 cells. Oncogene 19, 1428–1436 (2000). [PubMed: 10723134]

37. Zhang ZG, Lambert CA, Servotte S, Chometon G, Eckes B, Krieg T, Lapiere CM, Nusgens BV, Aumailley M, Effects of constitutively active GTPases on fibroblast behavior. Cell Mol Life Sci 63, 82–91 (2006). [PubMed: 16378244]

38. Michaelson D, Silletti J, Murphy G, D'Eustachio P, Rush M, Philips MR, Differential localization of Rho GTPases in live cells: regulation by hypervariable regions and RhoGDI binding. J Cell Biol 152, 111–126 (2001). [PubMed: 11149925]

39. Boulter E, Garcia-Mata R, Guilluy C, Dubash A, Rossi G, Brennwald PJ, Burridge K, Regulation of Rho GTPase crosstalk, degradation and activity by RhoGDI1. Nat Cell Biol 12, 477–483 (2010). [PubMed: 20400958]

40. Rolli-Derkinderen M, Sauzeau V, Boyer L, Lemichez E, Baron C, Henrion D, Loirand G, Pacaud P, Phosphorylation of serine 188 protects RhoA from ubiquitin/proteasome-mediated degradation in vascular smooth muscle cells. Circ Res 96, 1152–1160 (2005). [PubMed: 15890975]

41. Strassheim D, Porter RA, Phelps SH, Williams CL, Unique in vivo associations with SmgGDS and RhoGDI and different guanine nucleotide exchange activities exhibited by RhoA, dominant negative RhoA(Asn-19), and activated RhoA(Val-14). J Biol Chem 275, 6699–6702 (2000). [PubMed: 10702222]

42. Davis MJ, Ha BH, Holman EC, Halaban R, Schlessinger J, Boggon TJ, RAC1P29S is a spontaneously activating cancer-associated GTPase. Proc Natl Acad Sci U S A 110, 912–917 (2013). [PubMed: 23284172]

43. Poulin EJ, Bera AK, Lu J, Lin YJ, Strasser SD, Paulo JA, Huang TQ, Morales C, Yan W, Cook J, Nowak JA, Brubaker DK, Joughin BA, Johnson CW, DeStefanis RA, Ghazi PC, Gondi S, Wales TE, Iacob RE, Bogdanova L, Gierut JJ, Li Y, Engen JR, Perez-Mancera PA, Braun BS, Gygi SP, Lauffenburger DA, Westover KD, Haigis KM, Tissue-Specific Oncogenic Activity of KRAS(A146T). Cancer Discov 9, 738–755 (2019). [PubMed: 30952657]

44. Jin Y, Yu Y, Shao Q, Ma Y, Zhang R, Yao H, Xu Y, Up-regulation of ECT2 is associated with poor prognosis in gastric cancer patients. Int J Clin Exp Pathol 7, 8724–8731 (2014). [PubMed: 25674238]

45. Cook DR, Kang M, Martin TD, Galanko JA, Loeza GH, Trembath DG, Justilien V, Pickering KA, Vincent DF, Jarosch A, Jurmeister P, Waters AM, Hibshman PS, Campbell AD, Ford CA, Keku TO, Yeh JJ, Lee MS, Cox AD, Fields AP, Sandler RS, Sansom OJ, Sers C, Schaefer A, Der CJ, Aberrant Expression and Subcellular Localization of ECT2 Drives Colorectal Cancer Progression and Growth. Cancer Res 82, 90–104 (2022). [PubMed: 34737214]

46. Huff LP, Decristo MJ, Trembath D, Kuan PF, Yim M, Liu J, Cook DR, Miller CR, Der CJ, Cox AD, The Role of Ect2 Nuclear RhoGEF Activity in Ovarian Cancer Cell Transformation. Genes Cancer 4, 460–475 (2013). [PubMed: 24386507]

47. Justilien V, Ali SA, Jamieson L, Yin N, Cox AD, Der CJ, Murray NR, Fields AP, Ect2-Dependent rRNA Synthesis Is Required for KRAS-TRP53-Driven Lung Adenocarcinoma. Cancer Cell 31, 256–269 (2017). [PubMed: 28110998]

48. Solski PA, Wilder RS, Rossman KL, Sondek J, Cox AD, Campbell SL, Der CJ, Requirement for C-terminal sequences in regulation of Ect2 guanine nucleotide exchange specificity and transformation. J Biol Chem 279, 25226–25233 (2004). [PubMed: 15073184]

49. Jaiswal M, Dvorsky R, Ahmadian MR, Deciphering the molecular and functional basis of Dbl family proteins: a novel systematic approach toward classification of selective activation of the Rho family proteins. J Biol Chem 288, 4486–4500 (2013). [PubMed: 23255595]

50. Longenecker K, Read P, Lin SK, Somlyo AP, Nakamoto RK, Derewenda ZS, Structure of a constitutively activated RhoA mutant (Q63L) at 1.55 A resolution. Acta Crystallogr D Biol Crystallogr 59, 876–880 (2003). [PubMed: 12777804]

51. Chen M, Bresnick AR, O'Connor KL, Coupling S100A4 to Rhotekin alters Rho signaling output in breast cancer cells. Oncogene 32, 3754–3764 (2013). [PubMed: 22964635]

52. Watanabe N, Kato T, Fujita A, Ishizaki T, Narumiya S, Cooperation between mDia1 and ROCK in Rho-induced actin reorganization. Nat Cell Biol 1, 136–143 (1999). [PubMed: 10559899]

53. Blumenstein L, Ahmadian MR, Models of the cooperative mechanism for Rho effector recognition: implications for RhoA-mediated effector activation. J Biol Chem 279, 53419–53426 (2004). [PubMed: 15475352]

54. Rose R, Weyand M, Lammers M, Ishizaki T, Ahmadian MR, Wittinghofer A, Structural and mechanistic insights into the interaction between Rho and mammalian Dia. Nature 435, 513–518 (2005). [PubMed: 15864301]

55. Hahn WC, Counter CM, Lundberg AS, Beijersbergen RL, Brooks MW, Weinberg RA, Creation of human tumour cells with defined genetic elements. Nature 400, 464–468 (1999). [PubMed: 10440377]

56. Der CJ, Finkel T, Cooper GM, Biological and biochemical properties of human rasH genes mutated at codon 61. Cell 44, 167–176 (1986). [PubMed: 3510078]

57. Seeburg PH, Colby WW, Capon DJ, Goeddel DV, Levinson AD, Biological properties of human c-Ha-ras1 genes mutated at codon 12. Nature 312, 71–75 (1984). [PubMed: 6092966]

58. Bravo-Cordero JJ, Magalhaes MA, Eddy RJ, Hodgson L, Condeelis J, Functions of cofilin in cell locomotion and invasion. Nat Rev Mol Cell Biol 14, 405–415 (2013). [PubMed: 23778968]

59. Cox OT, O'Shea S, Tresse E, Bustamante-Garrido M, Kiran-Deevi R, O'Connor R, IGF-1 Receptor and Adhesion Signaling: An Important Axis in Determining Cancer Cell Phenotype and Therapy Resistance. Front Endocrinol (Lausanne) 6, 106 (2015). [PubMed: 26191041]

60. Hakuno F, Takahashi SI, IGF1 receptor signaling pathways. J Mol Endocrinol 61, T69–T86 (2018). [PubMed: 29535161]

61. Arias-Romero LE, Chernoff J, A tale of two Paks. Biol Cell 100, 97–108 (2008). [PubMed: 18199048]

62. Baker NM, Yee Chow H, Chernoff J, Der CJ, Molecular pathways: targeting RAC-p21-activated serine-threonine kinase signaling in RAS-driven cancers. Clin Cancer Res 20, 4740–4746 (2014). [PubMed: 25225063]

63. Clayton NS, Ridley AJ, Targeting Rho GTPase Signaling Networks in Cancer. Front Cell Dev Biol 8, 222 (2020). [PubMed: 32309283]

64. Chetty AK, Ha BH, Boggon TJ, Rho family GTPase signaling through type II p21-activated kinases. Cell Mol Life Sci 79, 598 (2022). [PubMed: 36401658]

65. Dupont S, Morsut L, Aragona M, Enzo E, Giulitti S, Cordenonsi M, Zanconato F, Le Digabel J, Forcato M, Bicciato S, Elvassore N, Piccolo S, Role of YAP/TAZ in mechanotransduction. Nature 474, 179–183 (2011). [PubMed: 21654799]

66. Park HW, Kim YC, Yu B, Moroishi T, Mo JS, Plouffe SW, Meng Z, Lin KC, Yu FX, Alexander CM, Wang CY, Guan KL, Alternative Wnt Signaling Activates YAP/TAZ. Cell 162, 780–794 (2015). [PubMed: 26276632]

67. He H, Snowball J, Sun F, Na CL, Whitsett JA, IGF1R controls mechanosignaling in myofibroblasts required for pulmonary alveologenesis. JCI Insight 6, (2021).

68. Sabra H, Brunner M, Mandati V, Wehrle-Haller B, Lallemand D, Ribba AS, Chevalier G, Guardiola P, Block MR, Bouvard D, beta1 integrin-dependent Rac/group I PAK signaling mediates YAP activation of Yes-associated protein 1 (YAP1) via NF2/merlin. J Biol Chem 292, 19179–19197 (2017). [PubMed: 28972170]

69. Xiao GH, Beeser A, Chernoff J, Testa JR, p21-activated kinase links Rac/Cdc42 signaling to merlin. J Biol Chem 277, 883–886 (2002). [PubMed: 11719502]

70. Calses PC, Crawford JJ, Lill JR, Dey A, Hippo Pathway in Cancer: Aberrant Regulation and Therapeutic Opportunities. Trends Cancer 5, 297–307 (2019). [PubMed: 31174842]

71. Nia HT, Munn LL, Jain RK, Physical traits of cancer. Science 370, (2020).

72. Zanconato F, Cordenonsi M, Piccolo S, YAP and TAZ: a signalling hub of the tumour microenvironment. Nat Rev Cancer 19, 454–464 (2019). [PubMed: 31270418]

73. Nguyen CDK, Yi C, YAP/TAZ Signaling and Resistance to Cancer Therapy. Trends Cancer 5, 283–296 (2019). [PubMed: 31174841]

74. Pattschull G, Walz S, Grundl M, Schwab M, Ruhl E, Baluapuri A, Cindric-Vranesic A, Kneitz S, Wolf E, Ade CP, Rosenwald A, von Eyss B, Gaubatz S, The Myb-MuvB Complex Is Required for YAP-Dependent Transcription of Mitotic Genes. Cell Rep 27, 3533–3546 e3537 (2019). [PubMed: 31216474]

75. Carboni JM, Wittman M, Yang Z, Lee F, Greer A, Hurlburt W, Hillerman S, Cao C, Cantor GH, Dell-John J, Chen C, Discenza L, Menard K, Li A, Trainor G, Vyas D, Kramer R, Attar RM,

Gottardis MM, BMS-754807, a small molecule inhibitor of insulin-like growth factor-1R/IR. Mol Cancer Ther 8, 3341–3349 (2009). [PubMed: 19996272]

76. Ndubaku CO, Crawford JJ, Drobnick J, Aliagas I, Campbell D, Dong P, Dornan LM, Duron S, Epler J, Gazzard L, Heise CE, Hoeflich KP, Jakubiak D, La H, Lee W, Lin B, Lyssikatos JP, Maksimoska J, Marmorstein R, Murray LJ, O'Brien T, Oh A, Ramaswamy S, Wang W, Zhao X, Zhong Y, Blackwood E, Rudolph J, Design of Selective PAK1 Inhibitor G-5555: Improving Properties by Employing an Unorthodox Low-pK a Polar Moiety. ACS Med Chem Lett 6, 1241–1246 (2015). [PubMed: 26713112]

77. Adeshakin FO, Adeshakin AO, Afolabi LO, Yan D, Zhang G, Wan X, Mechanisms for Modulating Anoikis Resistance in Cancer and the Relevance of Metabolic Reprogramming. Front Oncol 11, 626577 (2021). [PubMed: 33854965]

78. Mott HR, Owen D, Structures of Ras superfamily effector complexes: What have we learnt in two decades? Crit Rev Biochem Mol Biol 50, 85–133 (2015). [PubMed: 25830673]

79. Oh SC, Sohn BH, Cheong JH, Kim SB, Lee JE, Park KC, Lee SH, Park JL, Park YY, Lee HS, Jang HJ, Park ES, Kim SC, Heo J, Chu IS, Jang YJ, Mok YJ, Jung W, Kim BH, Kim A, Cho JY, Lim JY, Hayashi Y, Song S, Elimova E, Estralla JS, Lee JH, Bhutani MS, Lu Y, Liu W, Lee J, Kang WK, Kim S, Noh SH, Mills GB, Kim SY, Ajani JA, Lee JS, Clinical and genomic landscape of gastric cancer with a mesenchymal phenotype. Nat Commun 9, 1777 (2018). [PubMed: 29725014]

80. Choi W, Kim J, Park J, Lee DH, Hwang D, Kim JH, Ashktorab H, Smoot D, Kim SY, Choi C, Koh GY, Lim DS, YAP/TAZ Initiates Gastric Tumorigenesis via Upregulation of MYC. Cancer Res 78, 3306–3320 (2018). [PubMed: 29669762]

81. Zhang J, Wang G, Chu SJ, Zhu JS, Zhang R, Lu WW, Xia LQ, Lu YM, Da W, Sun Q, Loss of large tumor suppressor 1 promotes growth and metastasis of gastric cancer cells through upregulation of the YAP signaling. Oncotarget 7, 16180–16193 (2016). [PubMed: 26921249]

82. Unni AM, Lockwood WW, Zejnullahu K, Lee-Lin SQ, Varmus H, Evidence that synthetic lethality underlies the mutual exclusivity of oncogenic KRAS and EGFR mutations in lung adenocarcinoma. Elife 4, e06907 (2015). [PubMed: 26047463]

83. Miyoshi H, Stappenbeck TS, In vitro expansion and genetic modification of gastrointestinal stem cells in spheroid culture. Nat Protoc 8, 2471–2482 (2013). [PubMed: 24232249]

84. Wong GS, Zhou J, Liu JB, Wu Z, Xu X, Li T, Xu D, Schumacher SE, Puschhof J, McFarland J, Zou C, Dulak A, Henderson L, Xu P, O'Day E, Rendak R, Liao WL, Cecchi F, Hembrough T, Schwartz S, Szeto C, Rustgi AK, Wong KK, Diehl JA, Jensen K, Graziano F, Ruzzo A, Fereshetian S, Mertins P, Carr SA, Beroukhim R, Nakamura K, Oki E, Watanabe M, Baba H, Imamura Y, Catenacci D, Bass AJ, Targeting wild-type KRAS-amplified gastroesophageal cancer through combined MEK and SHP2 inhibition. Nat Med 24, 968–977 (2018). [PubMed: 29808010]

85. Schaefer A, Miertzschke M, Berken A, Wittinghofer A, Dimeric plant RhoGAPs are regulated by its CRIB effector motif to stimulate a sequential GTP hydrolysis. J Mol Biol 411, 808–822 (2011). [PubMed: 21723292]

86. Ly SH, Investigation of KRAS Dependency Bypass and Functional Characterization of All Possible KRAS Missense Variants Harvard University (2018). (https://dash.harvard.edu/handle/1/40050098).

87. Baldelli E, Calvert V, Hodge A, VanMeter A, Petricoin EF 3rd, Pierobon M, Reverse Phase Protein Microarrays. Methods Mol Biol 1606, 149–169 (2017). [PubMed: 28502000]

88. Signore M, Reeder KA, Antibody validation by Western blotting. Methods Mol Biol 823, 139–155 (2012). [PubMed: 22081344]

89. Baldelli E, Bellezza G, Haura EB, Crino L, Cress WD, Deng J, Ludovini V, Sidoni A, Schabath MB, Puma F, Vannucci J, Siggillino A, Liotta LA, Petricoin EF 3rd, Pierobon M, Functional signaling pathway analysis of lung adenocarcinomas identifies novel therapeutic targets for KRAS mutant tumors. Oncotarget 6, 32368–32379 (2015). [PubMed: 26468985]

90. Szklarczyk D, Gable AL, Nastou KC, Lyon D, Kirsch R, Pyysalo S, Doncheva NT, Legeay M, Fang T, Bork P, Jensen LJ, von Mering C, The STRING database in 2021: customizable protein-protein networks, and functional characterization of user-uploaded gene/measurement sets. Nucleic Acids Res 49, D605–D612 (2021). [PubMed: 33237311]

91. Jacomy M, Venturini T, Heymann S, Bastian M, ForceAtlas2, a continuous graph layout algorithm for handy network visualization designed for the Gephi software. PLoS One 9, e98679 (2014). [PubMed: 24914678]
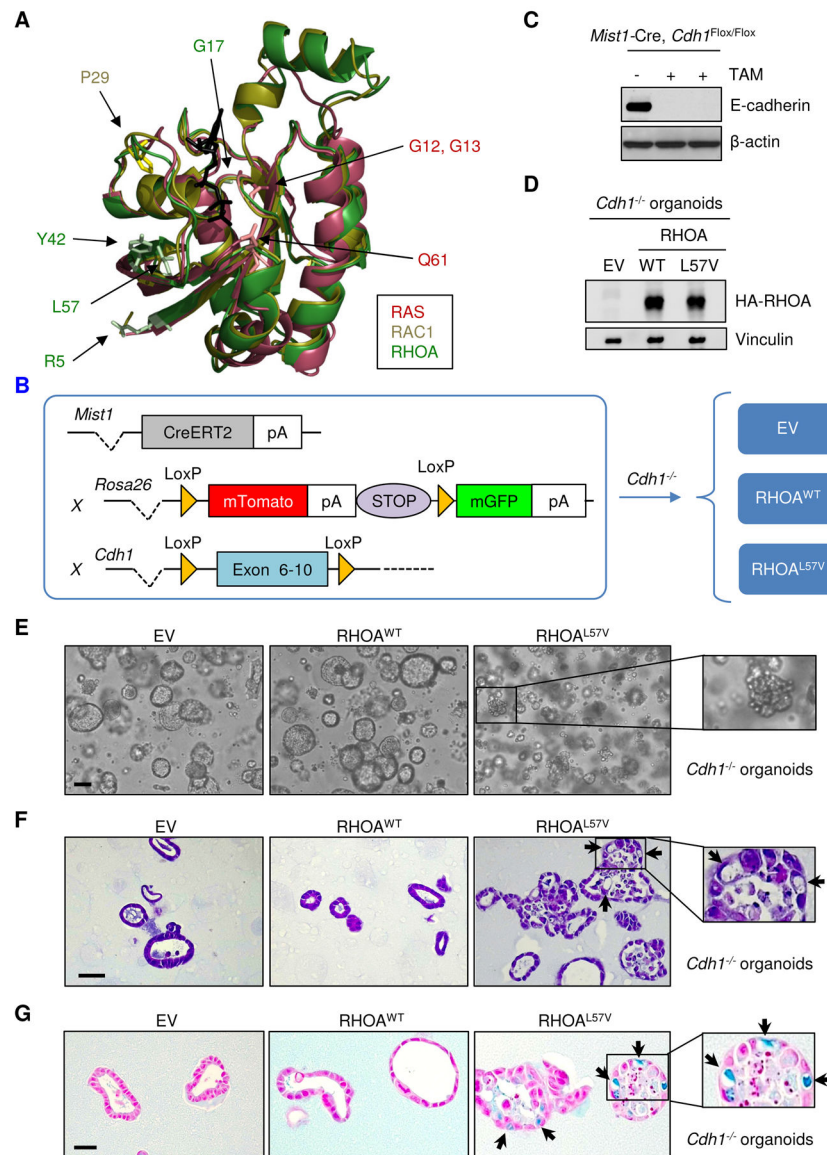
Fig. 1. RHOA^L57V disrupts gastric organoid morphology and induces a DGC-like phenotype.
(**A**) G-domain structure of RHOA [green, Protein Data Bank (PDB) ID: 1a2b], RAC1
(yellow, PDBID: 1mh1) and RAS (magenta, PDBID: 5p21) in the active confirmation is
shown as ribbon representation. Cancer-associated mutational hotspot residues are indicated
by color-coded sticks, the GTP-analog GTPγS by black sticks. (**B**) Schematic for the
generation of mice with the indicated genotypes, including the tomato-GFP reporter allele.
Isolated gastric organoids were treated with tamoxifen (TAM) in vitro to deplete *Cdh1*.
Cdh1^−/− organoids were then infected with the control lentivirus empty vector (EV) or
encoding HA epitope-tagged RHOA^WT or RHOA^L57V. (**C**) Immunoblot of *Cdh1* intact and
null isogenic organoids treated with or without TAM. (**D**) Immunoblot of *Cdh1*^−/− organoids
ectopically expressing EV, RHOA^WT or RHOA^L57V. Blots in (C and D) are representative
of three independent experiments. (**E to G**) Representative images of phase contrast (E),
hematoxylin and eosin (H&E; F) and alcian blue staining (G) of *Cdh1*^−/− organoids

expressing empty vector, RHOA^{WT} or RHOA^{L57V}. Arrows indicate cells resembling signet-ring cells (F) and cells with positive alcian blue staining (G). Images in (E to G) are representative of three independent experiments. Scale bars, 100 μm (E, F) and 50 μm (G).
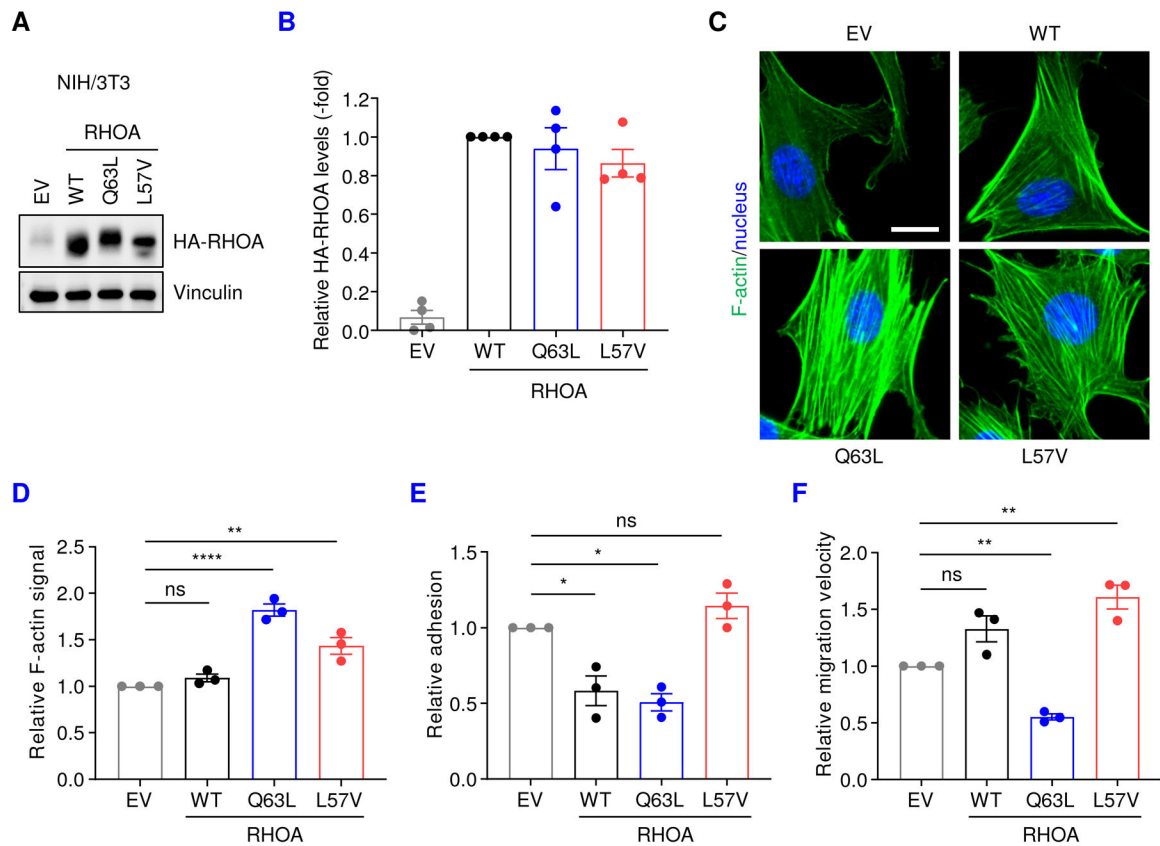
Fig. 2. RHOA^L57V is a gain-of-function mutant inducing stress fiber formation, cell adhesion and migration.

(**A**) Immunoblot analyses of NIH/3T3 fibroblasts stably expressing exogenous HA-tagged RHOA^WT, mutant or empty vector (EV). Vinculin was used to monitor equivalent total protein loading. (**B**) Quantitation of HA-RHOA protein levels in (A), normalized to loading control. Data are mean ± S.E.M. from four independent experiments. (**C**) Immunofluorescence analyses of NIH/3T3 fibroblasts expressing indicated RHOA variants or EV, stained with phalloidin (green) to detect F-actin stress fibers and DAPI (blue) as nuclear staining. Images are representative of three independent experiments. Scale bar, 20 μm. (**D**) Quantitation of F-actin stress fiber formation assays, representative images shown in (C). Data are mean ± S.E.M. from three independent experiments. ****$P < 0.0001$, **$P < 0.01$, ns, not significant by one-way ANOVA, Dunnett's multiple comparison test. Single cell data of an individual representative experiment are shown in fig. S1F. (**E**) CMFDA-labeled NIH/3T3 cells expressing the indicated RHOA variants or empty vector adhered for one hour on fibronectin-coated surfaces. (**F**) NIH/3T3 cells expressing indicated RHOA variants or EV were monitored during random migration for 16 hours using brightfield time-lapse microscopy (17 cells per condition). In (E and F) data are mean ± S.E.M. from three independent experiments. **$P < 0.01$, *$P < 0.05$, ns, not significant by one-way ANOVA, Dunnett's multiple comparison test.
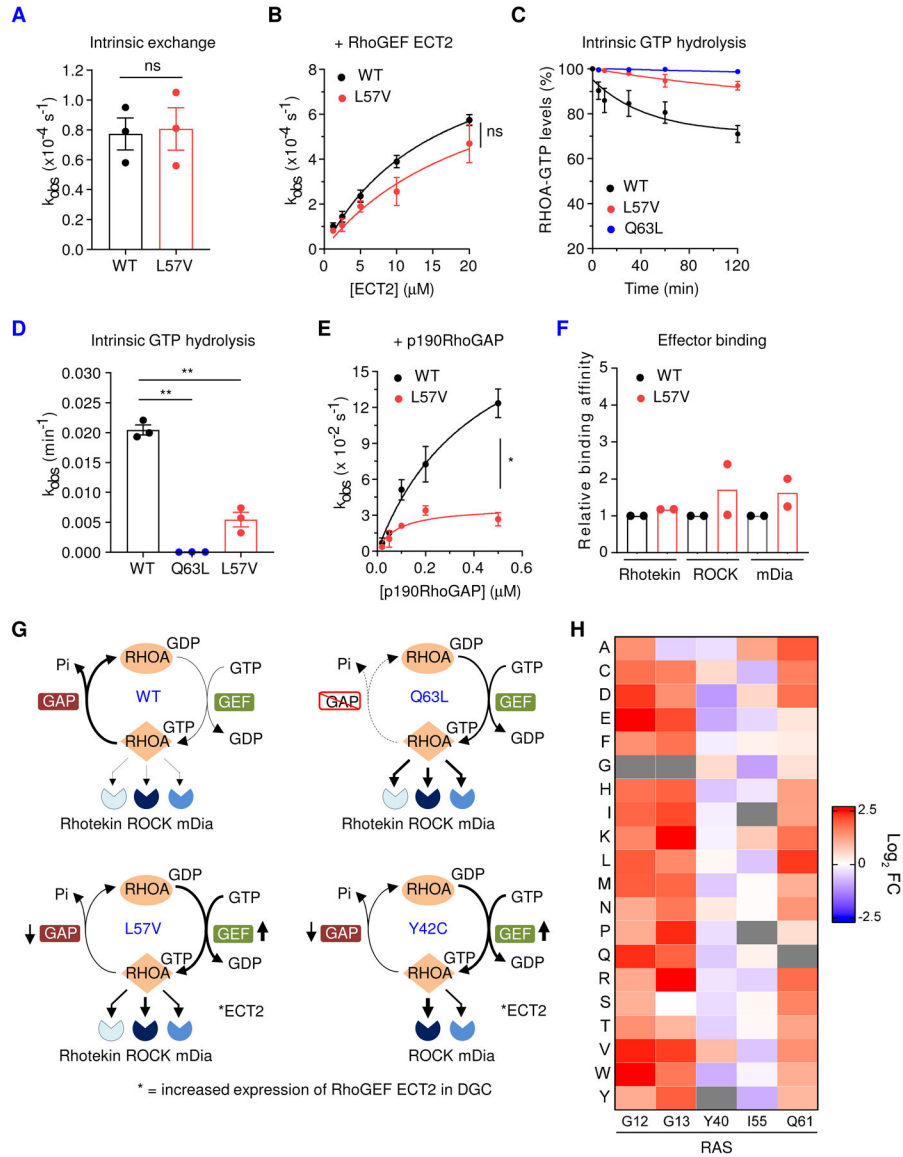
Fig. 3. RHOA[L57V] exhibits impaired GTP hydrolysis.

(**A**) Intrinsic nucleotide exchange activity of *E. coli* expressed recombinant RHOA[WT] and RHOA[L57V]. (**B**) Recombinant ECT2 catalytic PH-DH domain-mediated stimulation of RHOA nucleotide exchange activity. (**C and D**) Intrinsic GTP hydrolysis activity of recombinant RHOA was determined by RHOA-GTP levels in HPLC studies, with observed rates (k_{obs}) shown in (**D**). (**E**) Recombinant p190RhoGAP catalytic domain-mediated stimulation of RHOA GTP hydrolysis was detected by phosphate release using the phosphate binding protein sensor. Data in (A to E) are mean ± S.E.M. from three experiments. **$P < 0.01$, *$P < 0.05$, ns, not significant by unpaired *t*-test. (**F**) Normalized binding affinities of recombinant RHOA[WT] and RHOA[L57V] to RBD domains of indicated effectors, as measured in effector nucleotide dissociation studies. Affinities were normalized to RHOA[WT] interaction to each effector. Data are shown from two independent experiments; bars are means. (**G**) Comparison of the biochemical properties RHOA[WT], RHOA[Q63L]

and the oncogenic Y42C and L57V alterations in DGC. The Q63L mutation impairs intrinsic and RhoGAP-mediated GTP-GDP hydrolysis activities and enhances the nucleotide exchange of RHOA, favoring formation of nearly persistently GTP-bound, active RHOA. RHOA^{L57V} and RHOA^{Y42C} exhibit decreased intrinsic and RhoGAP-mediated GTP-GDP hydrolysis activities, but faster activities than RHOA^{Q63L}. In addition, many RHOA-specific GEFs such as ECT2 are overexpressed (indicated by *) in DGC, leading to enhanced levels of active GTP-bound RHOA^{L57V} or RHOA^{Y42C}. This increase is less compared than seen with RHOA^{Q63L}. RHOA^{Y42C} also shows altered effector binding. The thickness of the lines illustrates the level of activity/binding (impaired activity/binding, broken line; increased activity/binding, thick line). (**H**) Heatmap representation of the results of a positive-selection screen in HA1E cells expressing the indicated missense *KRAS* mutations. Cells were evaluated for their transforming activity. Columns represent the cancer-associated mutational hotspot KRAS residues G12, G13 and Q61, and the residues Y40 and I55, located at positions analogous to the cancer-associated *RHOA* mutations at Y42 and L57 (KRAS has two residues less than RHOA). Each row represents one of 20 possible amino acids (shown in one letter code). Relative allele abundance is shown as a Log_2 fold change (Log_2 FC) comparing the ultra-low attachment and the high attachment conditions after 7 days. Red indicates enrichment indicative of a gain-of-function phenotype and blue indicates depletion suggestive of a loss-of-function phenotype, as determined in HA1E cells. Gray coloration indicates alleles that were not included in the screening library.
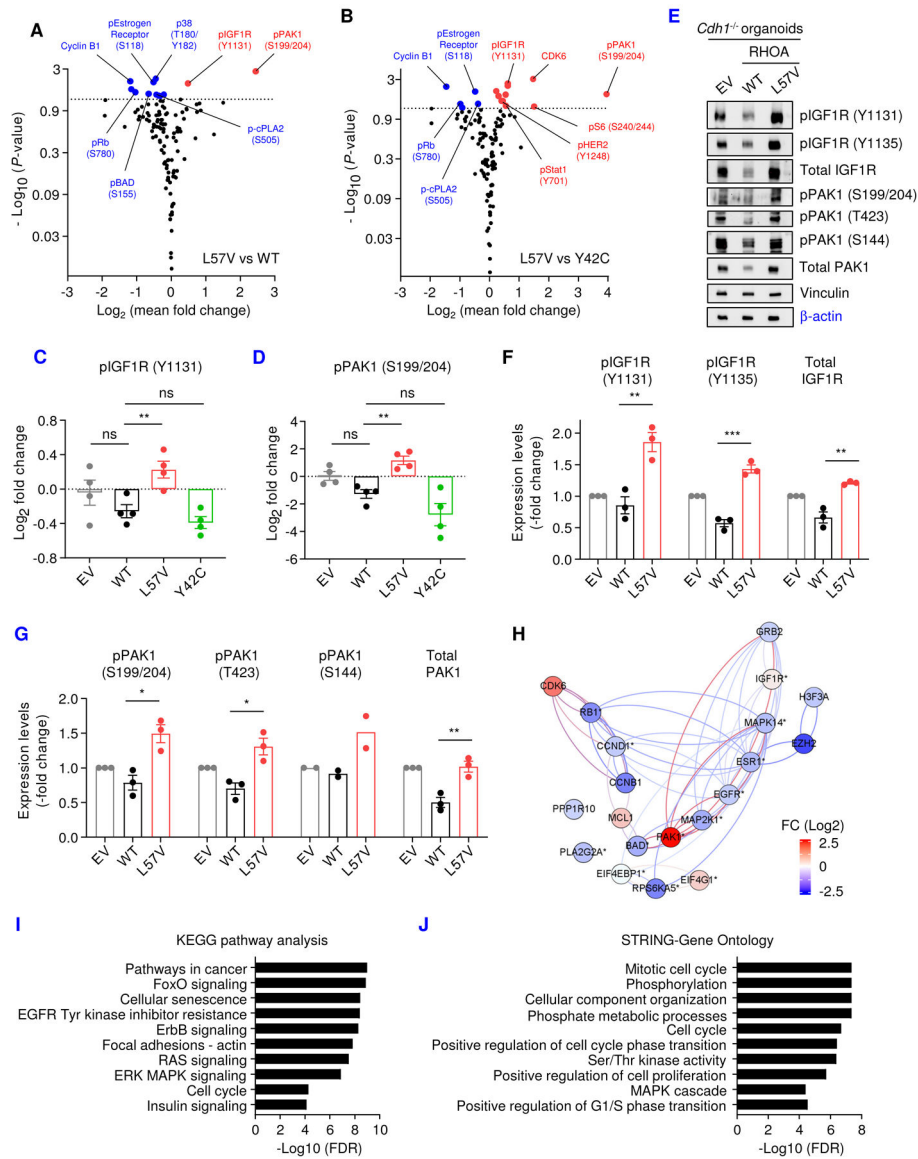
Fig. 4. RHOA[L57V] stimulates IGF1R and PAK1 signaling.

(**A and B**) Volcano plots show RPPA protein expression data comparing RHOA[L57V] with RHOA[WT] (A) and RHOA[Y42C] (B) expressing *Cdh1^{−/−}* organoids. Significantly upregulated (red) and downregulated (blue) proteins and phosphorylated proteins in RHOA[L57V] expressing organoids are highlighted. Horizontal dotted line represents $P < 0.05$ threshold (one-way ANOVA with Benjamin-Hochberg correction). Selected proteins are labeled. (**C and D**) Individual replicates of the RPPA analyses representing the levels of phosphorylated IGF1R (C) and PAK1 (D) in *Cdh1^{−/−}* organoids expressing WT or mutant RHOA or empty vector (EV). Data are mean ± S.E.M. from four biological replicates. $**P < 0.01$ and ns, not significant by one-way ANOVA with Benjamini-Hochberg correction. Data of the entire RPPA analyses are shown in fig. S3A. (**E**) Immunoblot of *Cdh1^{−/−}* organoids expressing WT or mutant RHOA or empty vector to assess levels of indicated proteins. Vinculin and β-actin were used as controls to monitor equivalent total protein loading. (**F and G**) Quantitation of

total and phosphorylated IGF1R (F) and PAK1 (G) as determined by immunoblot analyses represented in (E), normalized to the loading control (vinculin) and empty vector. Data are mean ± S.E.M. from three independent experiments (n = 2 for pPAK1 (Ser^{144})). ***P< 0.001, **P< 0.01, *P< 0.05 by unpaired t-test. (**H**) Gephi visualization of the STRING signaling interaction network of the top 20 hits of the volcano plot data in (A) representing the interaction network of the most upregulated (red) and downregulated (blue) proteins caused by RHOA^{L57V} expression, compared to RHOA^{WT}. Phosphorylated proteins indicated by *. Lines represent protein-protein interactions color-coded according to the average of the signal change between both proteins. FC, fold change. Genes and assigned protein names are listed in data file S1. (**I and J**) KEGG pathway (I) and Gene Ontology signaling (J) analyses of the top 20 hits of the volcano plot data in (A) indicating the most altered signaling pathways and biological processes in RHOA^{L57V} expressing $Cdh1^{-/-}$ organoids. FDR, false discovery rate.
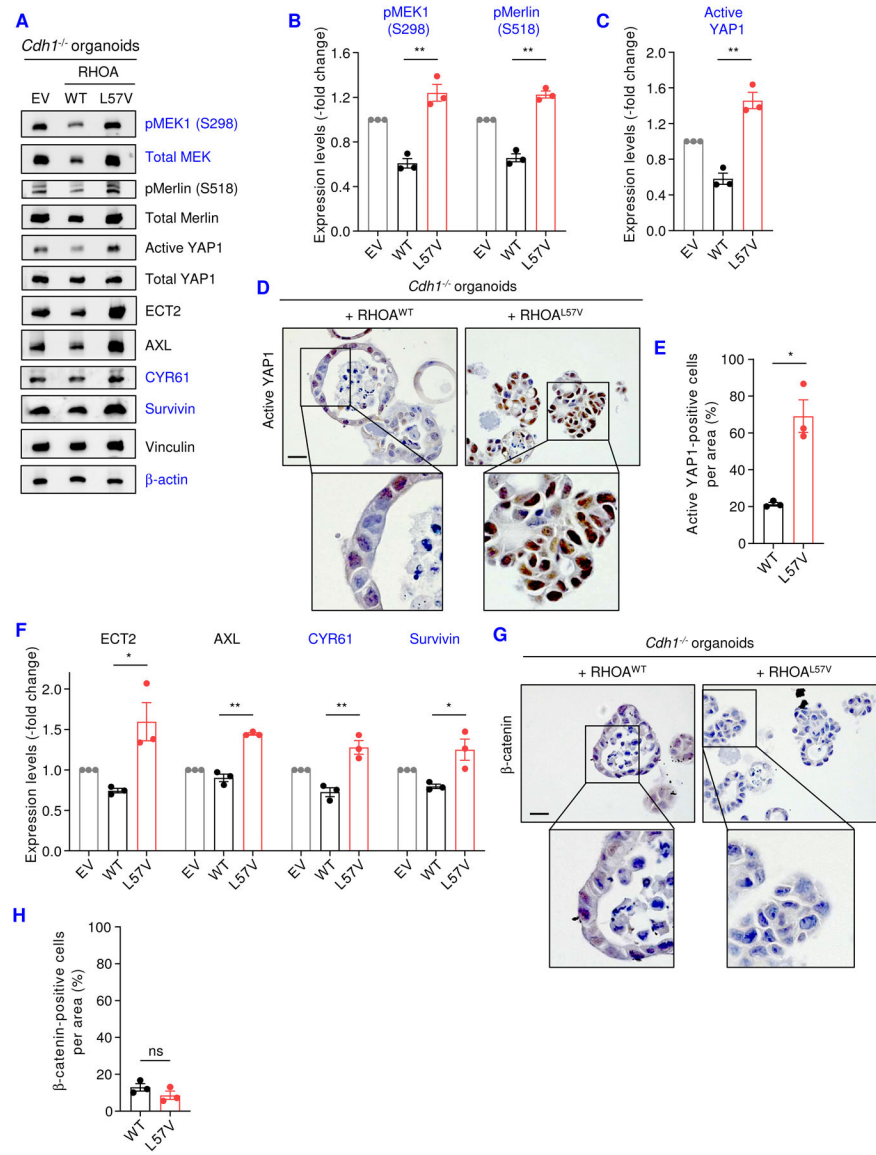
Fig. 5. RHOA^L57V promotes YAP1 signaling.
(**A**) Immunoblot analyses of *Cdh1^−/−* organoids expressing RHOA WT, mutant or empty vector (EV) control to assess levels of the indicated proteins. Vinculin and β-actin were used as controls to monitor equivalent total protein loading. (**B and C**) Quantitation of the immunoblot analyses (A) for indicated PAK1 substrates (B) and active YAP1 (C), normalized to the vinculin (loading control) and empty vector. (**D and E**) Representative IHC images of active YAP1 staining (D) and quantitation (E) of active YAP1-positive *Cdh1^−/−* organoids expressing RHOA^WT and RHOA^L57V. (**F**) Quantitation of the immunoblot analyses shown in A for indicated YAP1 targets, normalized to vinculin (loading control) and empty vector. (**G and H**) Representative IHC images of β-catenin staining (G) and quantitation (H) of β-catenin-positive *Cdh1^−/−* organoids expressing RHOA^WT and RHOA^L57V. (**B, C, E, F and H**) Data are mean ± S.E.M. from three

independent experiments. *$P < 0.05$, **$P < 0.01$ and ns, not significant by unpaired t-test (B, C and F) or Mann-Whitney test (E and H). Scale bars, 50 μm (D and G).
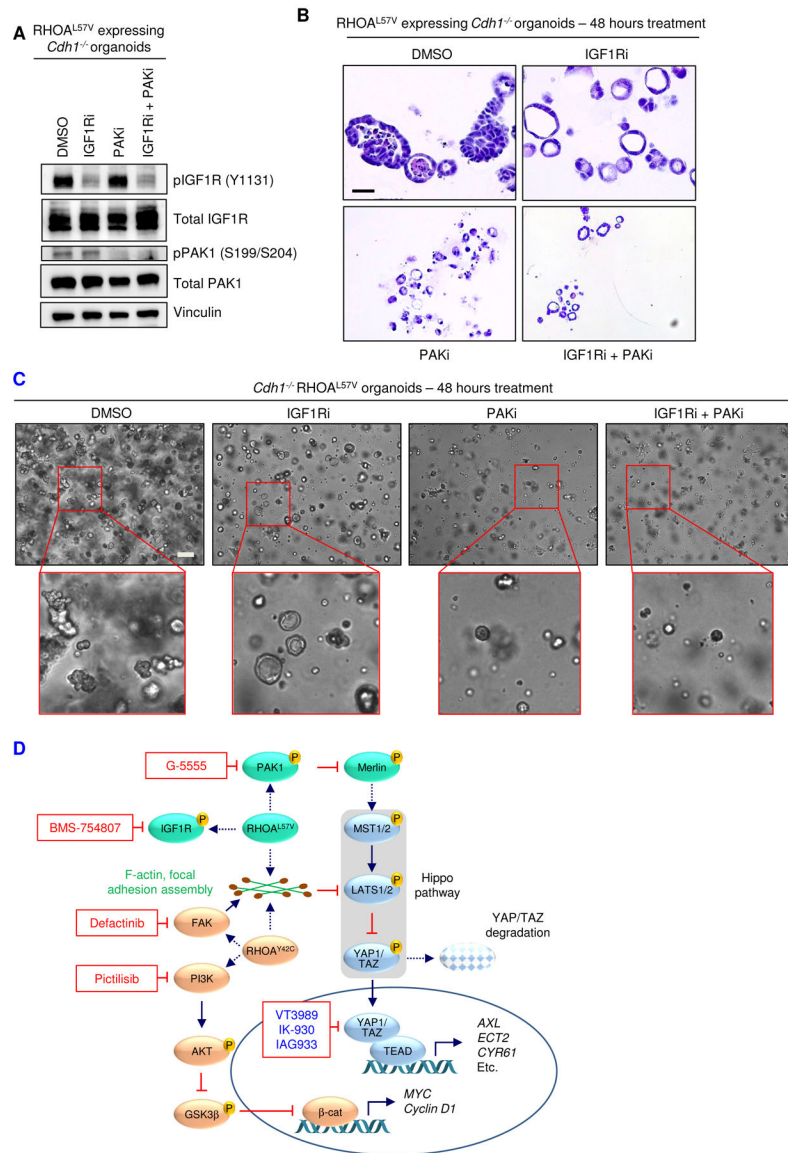
Fig. 6. RHOA^{L57V} expressing *Cdh1$^{-/-}$* organoids are sensitive toward pharmacologic inhibition of IGF1R and PAK.

(**A**) Immunoblot analyses of *Cdh1$^{-/-}$* organoids ectopically expressing RHOA^{L57V} treated for 24 hours with vehicle (DMSO), the IGFR1 inhibitor BMS-754807 (200 nM), the group I PAK-selective inhibitor G-5555 (200 nM), or in combination (each 200 nM). Vinculin was used as a control for equivalent total protein loading. Blots are representative of two independent experiments. (**B and C**) Representative H&E (B) and phase-contrast images (C) of *Cdh1$^{-/-}$* organoids ectopically expressing RHOA^{L57V} treated for 48 hours with vehicle control (DMSO), or with the IGF1R inhibitor BMS-754807 (200 nM) and/or PAK inhibitor G-5555 (200 nM). Images are representative of two independent experiments. Scale bars, 100 μm (B) or 200 μm (C). (**D**) RHOA^{Y42C} and RHOA^{L57V} signaling and convergence on YAP1. We showed previously that RHOA^{Y42C} caused FAK, and PI3K-AKT-GSK3β, and YAP1 activation to drive DGC oncogenic progression (23). In this study, we determined that RHOA^{L57V} caused IGF1R and PAK1 activation, and Merlin inhibition.

Merlin is an upstream activator of the MST1/2-LATS1/2 Hippo kinase cascade, leading to YAP1 phosphorylation and cytoplasmic sequestration and proteasomal degradation. The indicated inhibitors blocked mutant RHOA-driven DGC progression. Both RHOA mutants also stimulated ROCK-mediated F-actin and focal adhesion assembly, leading to YAP1 transcriptional co-activator activation. Dephosphorylated and activated YAP1 translocates to the nucleus where it forms a complex with the TEAD transcription factor. Solid and dotted line arrows indicate direct and indirect connections, respectively.